Journal of Building Engineering 111 (2025) 113331

Contents lists available at ScienceDirect

Journal of Building Engineering

journal homepage: www.elsevier.com/locate/jobe

The impact of courtyard roof shape on adjacent building natural ventilation and passive cooling

Hao Sun [a,*], Rafik Bensalem [b], Abdullah Dik [a,c,d], Zhu Tao [a], Zhe Wang [a], Carlos Jimenez-Bescos [e], John Kaiser Calautit [a]

[a] Department of Architecture and Built Environment, University of Nottingham, UK
[b] LRA Laboratory, National School of Architecture of Toulouse, France
[c] School of Engineering, University of Derby, UK
[d] Faculty of Engineering and Natural Sciences, Iskenderun Technical University, Iskenderun, Hatay, Türkiye
[e] Westminster Business School, University of Westminster, UK

ARTICLE INFO

Keywords:
Courtyard buildings
Computational fluid dynamics (CFD)
Roof shapes
Aero-thermal performance
Natural ventilation
Built environment
Wind tunnel
Passive cooling
Single-sided ventilation
Indoor environment

ABSTRACT

Do all courtyard shapes perform equally? This study investigates how different roof styles impact natural ventilation and passive cooling in courtyard buildings. However, previous analyses have often overlooked a crucial factor: the interaction between the courtyard's outdoor environment and adjacent indoor spaces. Prior research have largely concentrated on the external wind and thermal conditions, overlooking the air exchange between indoor spaces and the courtyard. To address this research gap, the current study investigates the impact of different roof styles on natural ventilation and temperature regulation within single-sided ventilated courtyard buildings. Employing Computational Fluid Dynamics (CFD) simulations validated through wind tunnel experiments, the research investigates common roof configurations such as flat, dome, butterfly, parapet, Chinese curved, mansard, open gable, gambrel, shed, and reverse shed. Our results indicate that roof geometry significantly affects airflow patterns, pressure distribution, and thermal conditions, demonstrating that it can play a crucial role in enhancing or impeding natural ventilation. Notably, the streamlined design of the dome roof enhanced natural ventilation, providing 80 % higher indoor wind speed than the traditional flat roof and lowering the average indoor temperatures by up to 2.1 °C. Importantly, these ventilation patterns remain consistent across varying wind directions, confirming the robustness of the findings. In contrast, the parapet roof exhibits the least effective ventilation performance, with the highest average indoor temperature of 26.4 °C and the lowest average wind speed. The analysis underscores that not all courtyard shapes perform equally. The dome and shed roofs are identified as better designs for enhancing natural ventilation and achieving more uniform temperature distributions across the indoor spaces.

* Corresponding author.
E-mail address: Hao.Sun1@nottingham.ac.uk (H. Sun).

https://doi.org/10.1016/j.jobe.2025.113331
Received 29 December 2024; Received in revised form 20 June 2025; Accepted 25 June 2025
Available online 27 June 2025

Abbreviation

ABL	Atmospheric Boundary Layer
CFD	Computational Fluid Dynamics
FVM	Finite Volume Method
GCI	Grid Convergence Index
LES	Large Eddy Simulation
RANS	Reynolds-Averaged Navier-Stokes
SIMPLE	Semi-Implicit Method for Pressure-Linked Equations

1. Introduction

Courtyards have long been regarded as dynamic social spaces that nurture community engagement and enrich urban landscapes [1,2]. These areas, which transcend time and culture, have evolved in terms of architectural style, reflecting the diversity of heritage and the environmental adaptations from ancient to modern times. In addition to their societal advantages, courtyards are also valued for allowing the penetration of natural light and promoting natural ventilation, thus enabling passive cooling in residential buildings [3,4]. However, despite their longstanding role in urban architecture, there remains a lack of investigation into how various design elements of courtyard buildings, particularly roof designs, affect airflow and heat distribution inside the surrounding rooms [5]. The layout, orientation, roof shape, and the strategic placement of openings in courtyard buildings significantly influence the microclimate within these spaces. These architectural features collectively shape distinct airflow patterns that enhance natural ventilation performance both within the courtyard and in adjacent indoor areas [6–10]. As a result, indoor air quality is improved, and effective summer cooling through natural ventilation is achieved.

Compared to conventional building forms, courtyard buildings, due to their distinct architectural design, have a unique microclimate. Airflow within these spaces is largely affected by their layout rather than external wind conditions [11]. However, the complex relationship between architectural elements, particularly roof structures, and natural ventilation often receives insufficient attention. This relationship involves air exchange between the indoor spaces, the courtyard itself, and the outdoor environment. According to previous studies, the style and shape of the roof significantly influence wind conditions within buildings [12,13]. Roof design, therefore, plays a dual role: it is crucial for functional performance and contributes to aesthetic appeal and cultural significance. For instance, the curved roofs in Chinese architecture [14], the dome-shaped roofs of buildings in the Middle East [15], and the modern rooftops with parapets [16], all of which illustrate how roof design can be both a response to climate conditions and a reflection of cultural heritage.

Various factors influence the aero-thermal environment of courtyard buildings, and roof design plays a particularly critical role due to its impact on airflow and heat transfer. Among these, buildings with single-sided ventilation facing the courtyard present a unique condition where the interaction between roof geometry and indoor environment becomes more significant, but remains underexplored. To address this research gap, this research focuses on evaluating how different shapes of roofs in such buildings affect natural ventilation and the indoor environment, as shown in Fig. 1. The key research questions are raised in this paper: *Which roof styles effectively improve airflow movement and facilitate heat removal from internal rooms of courtyard buildings? Conversely, what styles might adversely affect these conditions?* The insights from this research are expected to enhance the understanding of aero-thermal performance within courtyard buildings, offering practical guidelines for architectural design.

2. Literature review

In recent years, courtyard buildings have attracted growing academic attention due to their potential for improving thermal comfort and promoting passive ventilation in urban settings. Unlike other building typologies, courtyard structures establish a microclimatic buffer zone that modulates airflow, solar exposure, and temperature distribution within interior and semi-outdoor spaces. These environmental benefits, however, are not only dependent on the presence of a courtyard but also on the interaction between specific architectural factors such as geometry, spatial configuration, materiality, and roof design.

A substantial body of research has examined how layout and spatial parameters affect microclimatic performance in courtyards. Studies have highlighted that courtyard shape, orientation, and the selection of wall or ground materials influence airflow behaviour, stack effects, and heat retention [5,6,10,17–23]. Vegetation and water features have also been shown to provide cooling benefits, particularly in arid and warm-humid climates [24], while strategic spatial configurations aligned with prevailing wind directions further enhance natural ventilation [25,26]. These findings support the view that courtyard performance is highly sensitive to geometric and ecological design decisions.

Beyond geometry and landscape, recent studies have also addressed thermal management and pollutant dispersion challenges in courtyard environments. Sun et al. [27] demonstrated that insufficient natural ventilation in compact courtyard configurations can significantly elevate the risk of pollutant cross-transmission. In response, later studies have explored a range of passive design strategies aimed at improving airflow distribution, including evaporative cooling systems and modifications to ground-floor elevation. These interventions have been shown to enhance both thermal comfort and ventilation efficiency, thereby contributing to a healthier and more stable indoor–outdoor air exchange environment [28,29]. In addition, research on wall porosity and thermal inertia has revealed their dual role in enhancing air exchange while stabilising internal temperatures [2,30].

A key distinction in courtyard ventilation research lies in the comparison between single-sided and cross-ventilation strategies.

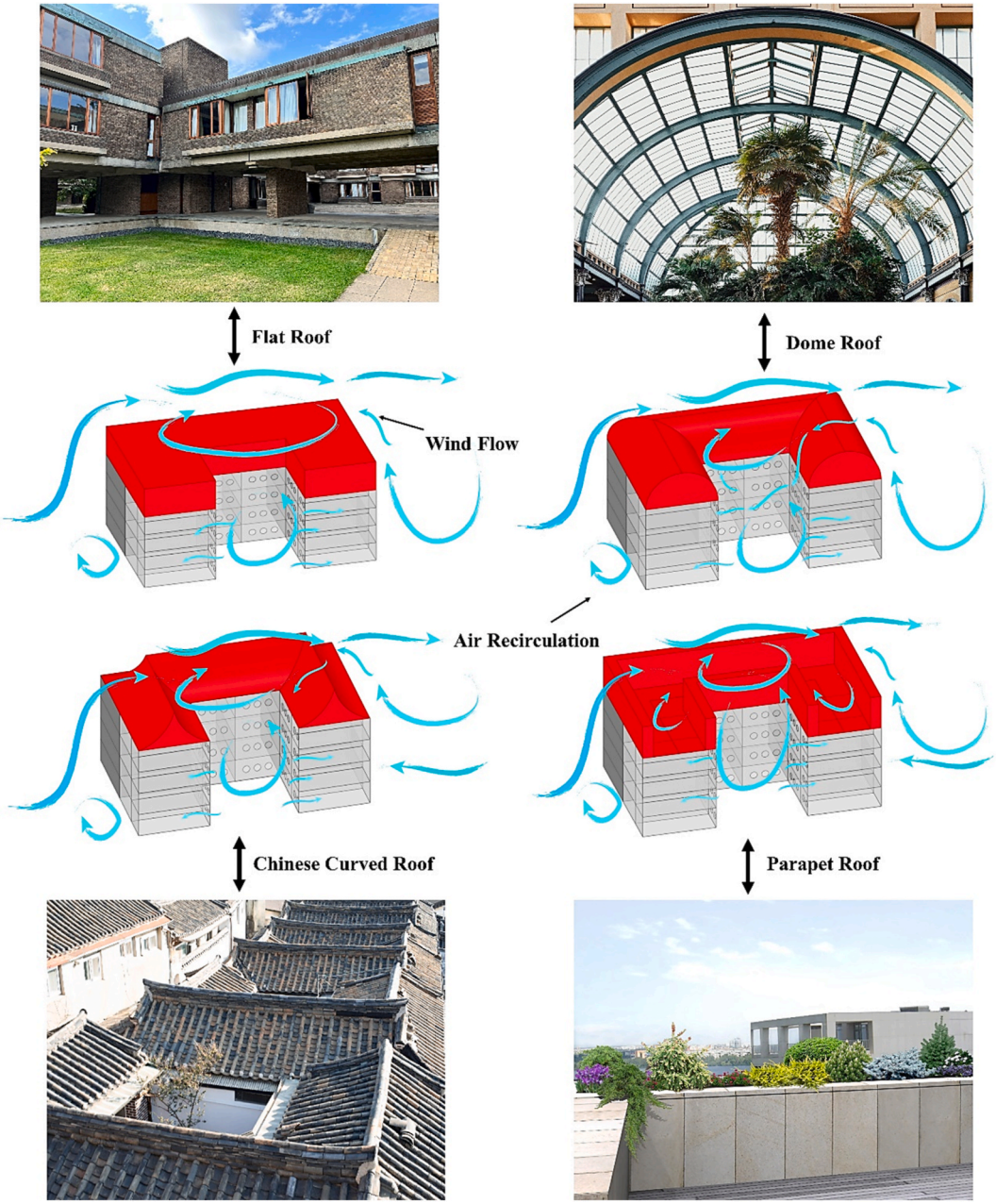

Fig. 1. Illustration of airflow movements through courtyard-facing openings in single-sided ventilated courtyard buildings with various roof styles.

While cross-ventilation is generally more effective in facilitating airflow and thermal comfort [31–34], it often requires continuous airflow paths across opposing façades, which may not be feasible in real-world residential layouts. In contrast, single-sided ventilation, though less effective overall, remains highly relevant to courtyard settings where internal partitions or limited façade exposure restrict crossflow. Several studies emphasise that single-sided ventilation performance is more dependent on architectural interventions such as opening placement and roof form [28,32,33]. This observation justifies a focused investigation of single-sided ventilation in the context of courtyard buildings.

Given the architectural constraints associated with single-sided ventilation, researchers have increasingly explored roof design as a means to optimise airflow and thermal regulation. Asfour and Gadi [35] reported that vaulted roofs improve internal air circulation by redistributing flow toward central and upstream zones. Similar findings were made for dome and curved roof types, although their ventilation effectiveness was shown to vary depending on wind direction. Other researchers have compared different leeward sawtooth, pitched, and hybrid roof geometries, demonstrating that shape and slope significantly influence pressure zones, airflow

paths, and pollutant dispersion [36–39]. Notably, steep roof pitches have been associated with higher air velocities near openings, while convex and straight profiles outperformed concave alternatives in enhancing indoor air velocity [36,37]. Prakash [38] further noted that pitched roofs, when combined with wider courtyard layouts, led to a 42 % improvement in ventilation efficiency compared to non-courtyard counterparts. Beyond geometry, roof-based shading and cooling strategies have also been explored. Zhu et al. [22] reviewed roof shading strategies in courtyard buildings, highlighting green roofs, canopies, and trellises as effective for reducing overheating and improving microclimate. Khan et al. found that roof openings enhance night-time ventilation, while shading elements like galleries can improve thermal comfort by up to 60 %, with courtyard width also influencing effectiveness [40].

In addition to geometry and shading strategies, the choice of roof material in courtyard buildings plays a critical role in daylight access and energy performance [41]. Yang et al. [42] showed that covering open courtyards with transparent roofing can reduce annual energy use by 53 % and improve thermal comfort by 39 % compared to traditional designs. The energy performance of roofed courtyards largely depends on the roof's light transmittance. High-transparency materials help capture solar heat and raise indoor temperatures, reducing heat losses and ventilation-related energy demands in cold climates [41]. However, in hot regions, they may cause overheating and increase cooling loads. Therefore, material selection must balance solar gain and thermal protection [41]. Li et al. examined enclosed courtyards with adjustable ventilated roofs, which improved thermal conditions in summer despite reduced winter daylight, highlighting the value of adaptive roof design [9].

Although previous studies have contributed important findings, their scope remains limited in several respects. Many investigations have focused exclusively on a single roof geometry or have been conducted in contexts that do not involve courtyard configurations, such as standalone buildings or urban street canyons. Systematic evaluations that examine the combined effects of roof design, courtyard geometry, and wind direction under single-sided ventilation conditions are still relatively scarce. This gap in the literature is significant, as the interaction among these variables is expected to have a substantial impact on the aero-thermal performance of courtyard buildings.

3. Research motivation and objectives

3.1. Research gaps and novelty

In the previous research on courtyard buildings, the focus was placed on the characteristics of courtyards to explore the impact of courtyard geometry and various designs on the wind and thermal environment within courtyards. However, these studies often overlook the indoor environment surrounding the courtyard. Regarding the impact of roof styles on buildings, the existing research is mostly limited to individual buildings or urban blocks, focusing on the effects of different roof styles on the wind environment, airflow patterns, and pollutant dispersion inside the building. However, there is little attention paid to their impact on indoor thermal performance and temperature distribution. Moreover, these studies usually consider a few roof styles, which causes a lack of thorough analysis. Notably, there remains an absence of research on the application of different roof styles in courtyard architecture. In most of the courtyard-related research or simulations, the flat roof is the main object to study.

What is especially notable is the significant gap in research on the indoor wind and thermal environment of courtyard buildings. Thus, the aim of this study is to reveal how different roof styles affect the microclimate of courtyards and, in turn, affect the surrounding indoor environment. To clearly isolate the influence of courtyard design on adjacent indoor conditions, this study focuses on courtyard buildings with single-sided ventilation, where airflow depends entirely on the courtyard opening. Through an in-depth exploration of how different roof styles affect courtyard buildings and the surrounding indoor wind and thermal environments, this study contributes new perspectives and strategies to the design and optimisation of courtyard architecture. This aims to enhance the thermal performance and overall environmental quality of buildings, which fills the existing research gap.

3.2. Aim and objectives

In this study, CFD is applied to explore the impact of ten different roof styles on the indoor wind and thermal environment of courtyard buildings. These roof styles are shown in Fig. 2. The workflow of this study and the key research questions are presented in Fig. 3. To begin with, the CFD validation of courtyard buildings is conducted by comparing with wind tunnel experiment data to determine the most appropriate turbulence model. Then, the validated CFD model is used to conduct a simulation analysis of the courtyard buildings with ten different roof styles.

By analysing the simulation results, this study aims to address five key research questions. The first theme investigates how different roof configurations influence wind patterns in courtyards and adjacent indoor spaces. The second examines whether natural ventilation performance remains consistent across varying wind directions (0°, 30°, and 45°) for different roof types. The third evaluates which roof style best enhances indoor natural ventilation. The fourth explores how roof geometry affects the ability of natural ventilation to dissipate indoor heat, based on a fixed indoor heat flux. Finally, the fifth analyses the relationship between courtyard wind behaviour and indoor airflow dynamics, particularly how they drive air movement through single-sided openings.

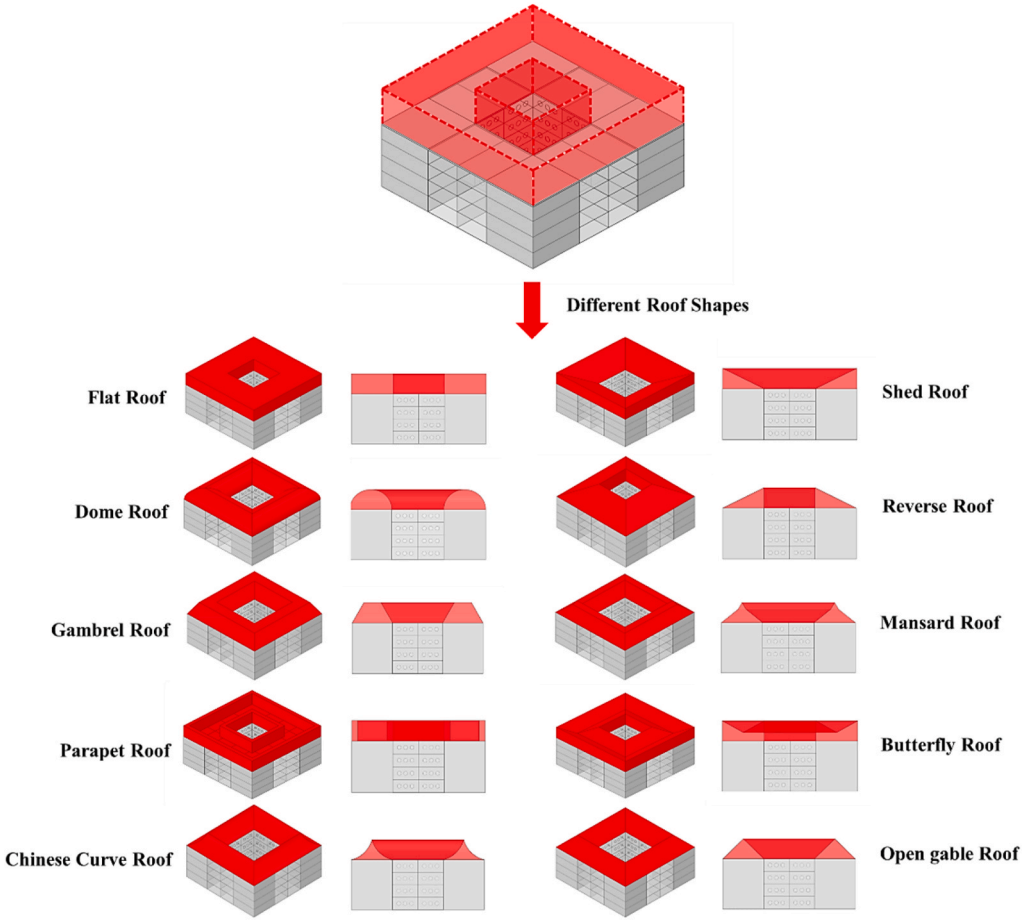

Fig. 2. Single-sided ventilated courtyard buildings featuring ten different roof styles.

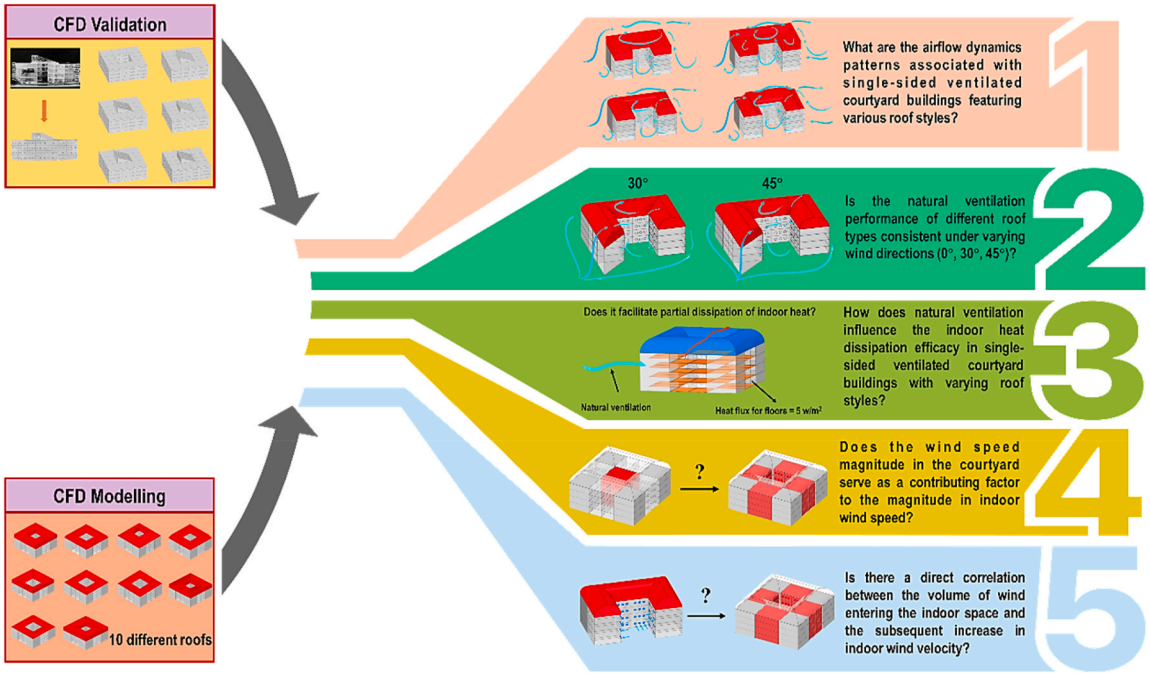

Fig. 3. The primary research workflow of the study and the five main research questions are addressed.

4. Method

In this section, a brief description of the wind tunnel experimental setup is first introduced to support CFD validation and ensure physical relevance. Then, an investigation was conducted by analysing the fundamental principles of CFD and defining the solver settings. The courtyard model was elaborated on, including its dimensions, structural composition, and implementation under the simulation framework. The fluid domain setup was then detailed, involving the spatial extent and critical attributes of fluid flow. Besides, the grid design was introduced in detail, focusing on its type, dimensions, and allocation methodology, to capture the intricate phenomena via an optimised grid layout. The reliability and precision of the simulation results were determined through a mesh independence test. Lastly, the boundary conditions were finalised through simulation, covering the fluid inlet and outlet parameters, along with other critical physical boundary specifications.

4.1. Wind tunnel experimental setup

The wind tunnel experiments used for CFD validation were originally conducted by Bensalem [43], with additional methodological details provided by Sharples and Bensalem [44]. The tests were performed in a closed-circuit atmospheric boundary layer wind tunnel with a working section of 7.2 m in length and 1.2 × 1.2 m in cross-section. The overall experimental setup and wind tunnel conditions are illustrated in Fig. 4, adapted based on the description by Bensalem [43]. The flow velocity was typically set to 25 m/s, resulting in a reference wind speed of approximately 16.4 m/s at eaves height, enabling the achievement of a sufficiently high Reynolds number for aerodynamic similarity.

To simulate a suburban outdoor environment, upstream flow conditioning elements, including spires, roughness blocks, and a castellated fence, were used. These generated a boundary layer with a height of 800 mm and a velocity profile following a power-law exponent of 0.245. Two wind directions, 0° (normal) and 45° (oblique), were examined.

The model was mounted at the centre of a 1.1 m diameter turntable to allow wind direction adjustment. All tests were conducted after 1 h of stabilisation to ensure steady boundary conditions. Airflow through the courtyard building models was measured using a calibrated orifice plate installed within one of the modular Perspex blocks, as described in Bensalem [43]. The pressure drop across the orifice was recorded using a digital micromanometer, allowing indirect calculation of volumetric flow rates. Reference calibration was performed against a commercial flowmeter traceable to national standards.

As illustrated in Fig. 4, measurements were taken at centrally located positions on each floor and façade of the model to capture representative airflow distribution. Differential pressure readings were obtained using FC 012 micromanometers, which have a stated precision of 1 %. Each device was recalibrated prior to use to minimise measurement drift. In addition, the reference wind speed was determined from dynamic pressure readings at the boundary layer height of 800 mm using a pitot-static tube. The estimated uncertainty in flow measurements was approximately ±10 %, primarily due to fluctuations in pressure signals [43,44].

To ensure the aerodynamic relevance of the scaled wind tunnel experiments, similarity criteria were carefully considered. Although the physical models were constructed at a scale of 1:100, larger than the flow field scaling ratio of approximately 1:350, this choice was necessary to accommodate internal orifice plate instrumentation and to achieve sufficiently high Reynolds numbers [43]. According to Bensalem [43] and Cermak et al. [45], internal ventilation flow similarity is primarily governed by Reynolds number independence rather than strict geometric matching. The experiments achieved Reynolds numbers exceeding 2×10^3 for the pressure loss coefficient and 5×10^3 for the discharge coefficient, which are considered sufficient for flow independence.

Moreover, the Reynolds number based on building height (0.13 m) and the reference wind speed at eaves height (16.4 m/s) was

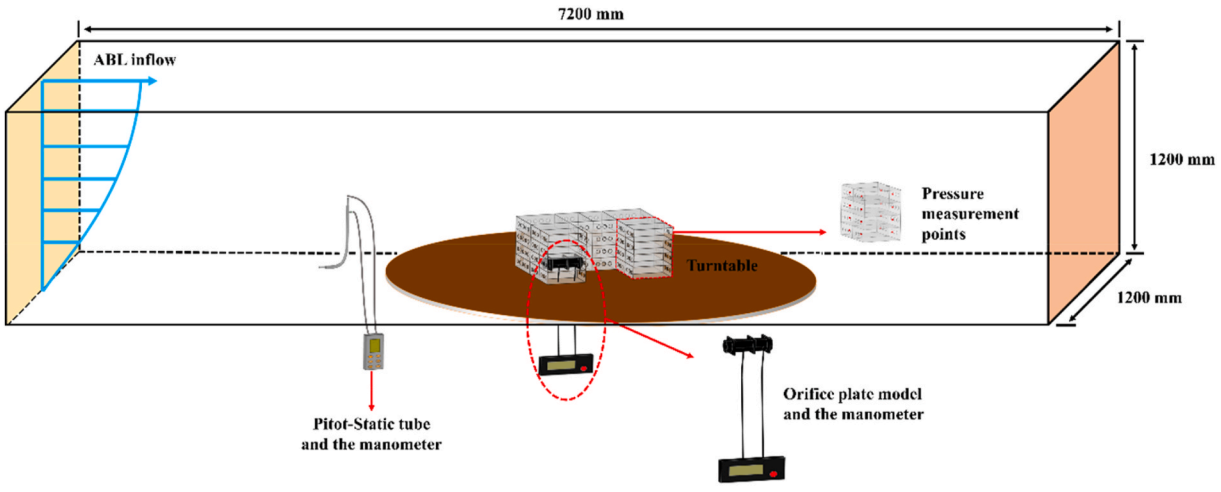

Fig. 4. Experimental setup highlighting airflow measurement instrumentation and model placement in the wind tunnel.

calculated as approximately 1.4×10^5. This value is well above the threshold of 3.3×10^4 proposed by Cui et al. [46] for achieving turbulent flow independence in similar urban boundary-layer studies. While minor overestimations (up to 12 %) may occur in limited cases where the dimensionless flow coefficient (CQ) drops below 0.25, the overall flow characteristics remain robust. By achieving and verifying these Reynolds numbers, our model under both 0° and 45° wind directions ensures that the flow behaviour corresponds closely to full-scale expectations, thereby adhering to the similarity criteria essential for accurate modelling and analysis.

4.2. CFD theory

CFD was adopted as the primary analysis method in this study, due to its proven ability to simulate airflow behaviour and thermal interactions in built environments with high spatial and temporal resolution. Compared to physical experiments or field measurements, CFD allows the systematic evaluation of multiple roof geometries, wind directions, and boundary conditions under consistent and controlled settings. This approach is particularly advantageous when exploring design variations in courtyard buildings, as it enables efficient parametric analysis without the time and cost constraints of wind tunnel testing or full-scale monitoring. Furthermore, CFD provides detailed insight into airflow patterns, pressure distribution, and temperature fields, which are often difficult to capture experimentally. The method has been successfully applied and validated in previous studies on natural ventilation and indoor-outdoor airflow in similar architectural contexts [2,27], supporting its reliability and relevance for the current investigation.

In this study, the control volume approach was adopted, with ANSYS Fluent 2021 software applied to perform steady-state Reynolds-Averaged Navier-Stokes (RANS) analysis of flow and mass fraction equations. The simulation, conducted in 3D CFD, considered a fully turbulent and incompressible flow. To close the RANS equations, the *k*-omega Standard model was applied and guided by the results of validation (detailed in Section 5). The CFD software applied in this study relies on the Finite Volume Method (FVM) and a semi-implicit algorithm to perform velocity-pressure coupling (SIMPLE), for second-order windward discrete pressure correlation equations. The convergence of the solution was achieved when the residuals of mass, momentum, and energy equations fell below 10^{-6}. The governing steady-state equations, as defined by the commercial CFD code ANSYS/Fluent [47], are expressed as follows:

Continuity equation:

$$\frac{\partial \rho}{\partial t} + \nabla \cdot (\rho \vec{v}) = 0 \tag{1}$$

where ρ represents the density, t denotes time, and $\vec{v}$ refers to the velocity vector.

Momentum equation:

$$\frac{\partial (\rho \vec{v})}{\partial t} + \nabla \cdot (\rho \vec{v} \vec{v}) = -\nabla p + \nabla \cdot \tau + \rho \vec{g} \tag{2}$$

where p represents pressure, τ indicates the stress tensor, and $\vec{g}$ denotes the gravitational acceleration vector.

Energy equation:

$$\frac{\partial}{\partial t}\left[\rho\left(e + \frac{v^2}{2}\right)\right] + \nabla \cdot \left[\rho v\left(h_f + \frac{v^2}{2}\right)\right] = \nabla \cdot \left(\kappa_{eff} \nabla T - \sum_j h_j \vec{J}_j + \tau_{eff} \cdot \vec{v}\right) + S_h \tag{3}$$

where e denotes the internal energy; h_f represents the mass-specific enthalpy, with only dry air considered; κ_{eff} indicates the effective thermal conductivity; T refers to the temperature of the air; h_j indicates the sensible heat of species j, while J denotes the diffusion flux of species j, both of which are excluded from this study; τ_{eff} indicates the effective stress tensor; and S_h refers to the volumetric heat source.

In this study, the performance of five commonly used turbulence models is evaluated through a wind tunnel experiment, which includes the *k*-epsilon Standard model [48], the *k*-epsilon RNG model [49], the *k*-epsilon Realisable model [50], the *k*-omega Standard model [51,52], and the *k*-omega SST model [53]. Based on the existing results shown in Appendix Table A.1 to Table A.5, the *k*-omega Standard model was taken as the primary model for subsequent research. This choice was made by considering the accuracy and efficiency demonstrated by the model in the simulation of wind tunnel experimental data.

The transport equations governing the *k*-omega Standard model are presented in Equations. (4) and (5):

Turbulence kinetic energy *k*:

$$\frac{\partial}{\partial t}(\rho k) + \frac{\partial}{\partial x_i}(\rho k u_i) = \frac{\partial}{\partial x_j}\left(\Gamma_k \frac{\partial k}{\partial x_j}\right) + G_k - Y_k + G_b \tag{4}$$

The specific dissipation rate ω:

$$\frac{\partial}{\partial t}(\rho \omega) + \frac{\partial}{\partial x_i}(\rho \omega u_i) = \frac{\partial}{\partial x_j}\left(\Gamma_\omega \frac{\partial \omega}{\partial x_j}\right) + G_\omega - Y_\omega + G_{\omega b} \tag{5}$$

In these two equations, G_k represents the generation of turbulence kinetic energy from mean velocity gradients; G_ω refers to the generation term for ω; Γ_k and Γ_ω denote the effective diffusivity of k and ω, respectively; Y_k and Y_ω represent the dissipation of k and ω due to turbulence; and G_b and $G_{\omega b}$ are the terms that take into account buoyancy effects.

4.3. Courtyard geometry, computational domain, and boundary conditions

Building upon the experimental courtyard model developed by Sharples and Bensalem [44], this study adopts the same geometric configuration but introduces modifications to the roof design in order to investigate the effects of single-sided ventilation. While retaining the original model scale and dimensions, the atrium roof was replaced with ten different roof shapes for comparative analysis. This approach enables a systematic evaluation of how roof geometry influences airflow performance under consistent architectural and boundary conditions.

As shown in Fig. 5 (a), the single-sided ventilated courtyard building under study has the same dimensions as the wind tunnel experiment described in Refs. [43,44]. With a length and width of 390 mm, they have four stories, each of which is 32.5 mm in height, which means a total height of 130 mm. The roof was uniformly set to 52 mm in height. The courtyard, which measured 130 mm × 130 mm x 130 mm, was located at the centre of the building. Considering single-sided ventilation inside the building, all openings pointed to the courtyard. To quantify the impact of the courtyard on the indoor wind and thermal environment of the surrounding buildings, this study focuses on the rooms facing the courtyard. Each floor had eight rooms facing the courtyard, with two adjacent rooms on each side. As shown in Fig. 5 (b), there were three circular openings with a diameter of 10 mm in each room, facing the courtyard.

Fig. 6 (a) shows the dimensions and configuration of the fluid domain, which is consistent with the wind tunnel experiment. To be exact, the length was 7200 mm and the cross section measured 1200 mm × 1200 mm. The spacing between the courtyard and symmetrical walls on both sides was set to 430.5 mm. The distance from the courtyard to the velocity inlet and pressure outlet was 2800 mm and 4061 mm, respectively. The distance from the courtyard to the top of the fluid domain was set to 1018 mm. Considering that the volume of the fluid domain in the wind tunnel experiments was relatively larger than in the courtyard building model, an embedded fluid domain was designed within the main fluid domain. Adjacent to the courtyard, as shown in Fig. 6 (b), it was maintained 200 mm from the courtyard's surfaces and roof. This is proposed to facilitate the effective transition of the grid. It measured 739 mm × 739 mm x 382 mm, whose a distance to the velocity inlet and pressure outlet of 2600 mm and 3861 mm, respectively. Thus, simulation precision was balanced with computational efficiency.

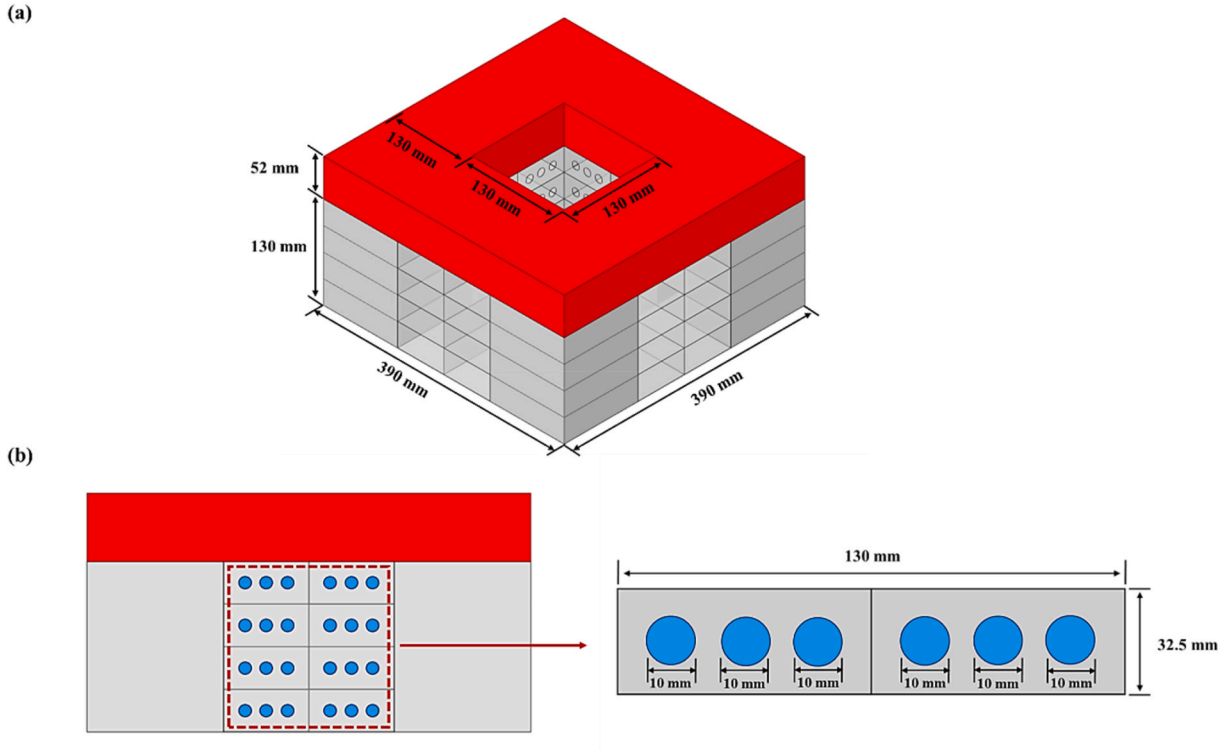

Fig. 5. (a) The dimension of the courtyard building and (b) cross-section of the building facing the courtyard, and the dimension of window opening.

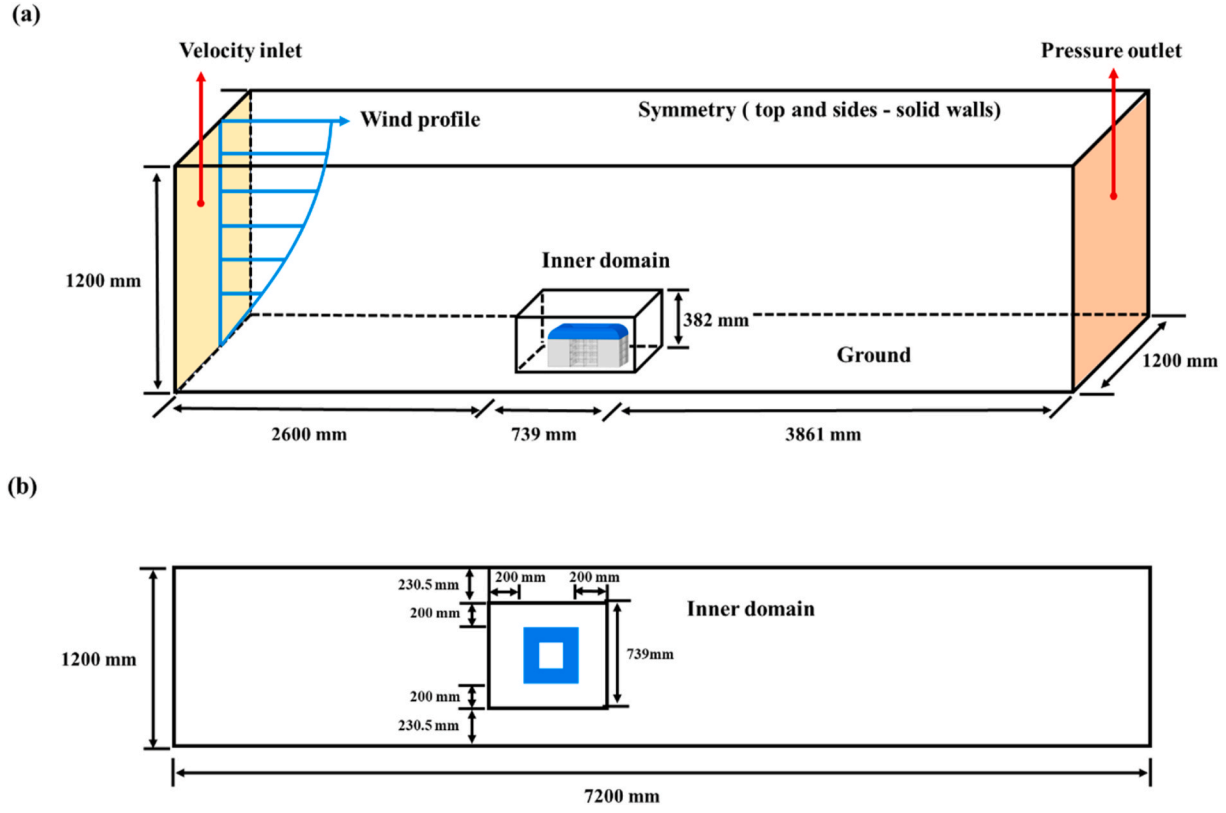

Fig. 6. (a) The dimension of the computational domain and the boundary conditions. (b) top view of the computational domain.

4.4. *Boundary conditions for the simulation study*

The configuration in Fig. 6 (a) requires designating a surface as the velocity inlet, where the wind speed distribution at this inlet is determined by referencing the atmospheric boundary layer (ABL) wind tunnel experiment, to model airflow within the computational domain [43,44]. Under all scenarios of simulation, the distribution of this inlet wind speed remained constant. The velocity profile, formulated in the power law expression, was obtained through a regression fit based on the velocity measurement performed at the centre of the turntable and at different heights. The mean velocity profile is expressed as follows:

$$u(z) = u_{ref}\left(\frac{z}{z_{ref}}\right)^{\alpha} \tag{6}$$

In the above equation, $u(z)$ denotes the mean velocity at height z, in m/s. The power law exponent α, determined as 0.245 through the wind tunnel experiment, is unique to such environments as suburban areas or urban terrains without significant high-rise structures [43]. It was derived from the curve-fitting wind tunnel results. The reference height z_{ref} , which was set to 800 mm, is aligned with the eaves level. Denoted as u_{ref} , the velocity experimentally measured at this reference height was recorded as 16.4 m/s [44]. Then, the specified wind speed distribution was implemented at the inflow boundary within the computational domain. The simulation was performed by following the same wind speed distribution as measured in the experiment. The boundary on the opposite side was treated as a pressure outlet and was maintained at a static pressure of 0 Pa.

This study was conducted based on the climate of Nottingham, UK (latitude 52.939°N, longitude 1.197°W). Similar to most parts of the UK, Nottingham features a temperate maritime climate, which is characterised by warm and mild summers and cool, mild winters. To conduct this study, the average temperature in Nottingham during a typical summer month, July 2021, which was 22 °C [54], was taken as the initial boundary condition for both the velocity inlet and pressure outlet settings. On this basis, the impact of natural ventilation on indoor air velocity and temperature was examined. The impact of relative humidity was not considered in this study for simplification.

In the process of CFD simulation, the effect of buoyancy was taken into consideration, and the gravity was fixed at $-9.81\ m/s^2$. Non-slip boundary conditions were determined for the symmetry of the top, two side walls, and the ground boundary. On this basis, the effectiveness of natural ventilation in removing heat from the single-sided ventilated courtyard building was explored. For this purpose, a uniform heat flux was created as an internal heat source on the floors of 32 experimental rooms facing the courtyard. Since the courtyard model adopted the same design as used in the wind tunnel experiment without proportional enlargement, the heat flux was applied only in the CFD simulation and set to a value of $5\ W/m^2$ to assess thermal performance under controlled indoor conditions [55].

4.5. Grid and sensitivity analysis

The accuracy of numerical simulation and the duration of computation are affected by mesh quality in the process of modelling. Under the context of ANSYS Meshing, a tetrahedral mesh was created for the fluid domain. To obtain accurate simulation results, two fluid domains were positioned around the courtyard model to optimise grid transition. These domains include an outer domain with a grid size of 100 mm and an inner domain with a grid size of 50 mm. In addition, mesh refinement was performed in the critical areas across the courtyard building. Specifically, the floors with heat flux were set to a grid size of 1.5 mm, while the circular window openings were set to a grid size of 0.8 mm. The roof, which was the focus of this study, was set to a grid size of 0.4 mm.

The external surface of the building was set to a grid size of 1 mm, while the remaining parts of the courtyard building were set to a grid size of 2 mm. In this way, the accuracy of simulation results was improved. The ratio of expansion for adjacent cells was maintained at a lower level than 1.2. To enhance computational efficiency and accelerate processing, the tetrahedral mesh of the fluid domain was transformed into a more efficient polyhedral mesh in ANSYS Fluent. To verify the accuracy of the numerical model, a mesh sensitivity analysis was performed by examining how the results varied with the change in mesh size. Discretisation uncertainty was assessed against the grid convergence index (GCI), as proposed in Ref. [56]. This analysis and the parameters involved in it are detailed below.

For the purpose of calculation, it's necessary to determine the grid size first, which is denoted as h. Herein, ΔV_i represents the volume, and N refers to the total number of cells used for the computation.

$$h = \left[\frac{1}{N}\sum_{i=1}^{N}(\Delta V_i)\right]^{1/3} \tag{7}$$

Fig. 7 and Table 1 show the process of choosing three grid sizes — fine, medium, and coarse. They were used in simulation to determine the value of critical variables (ϕ_1, ϕ_2, ϕ_3) required to achieve the research goals. The grid refinement factor, denoted as $r = h_{coarse}/h_{fine}$, is supposed to exceed 1.3 [56]. When $h_1 < h_2 < h_3$, the ratios are expressed as $r_{21} = h_2/h_1$, so that $r_{32} = h_3/h_2$. Accordingly, the grid sizes were set as N1 (15,889,281), N2 (6,783,437), and N3 (2,391,933), yielding the r values of 1.328 and 1.415. The effective order of this method, which is denoted as p, is calculated using Eq. (8) to Eq. (14), where $\varepsilon_{32} = \phi_3 - \phi_2$ and $\varepsilon_{21} = \phi_2 - \phi_1$.

$$p = \frac{1}{\ln(r_{21})}\left|\ln\left|\varepsilon_{32}/\varepsilon_{21}\right| + q(p)\right| \tag{8}$$

$$q(p) = \ln\left(\frac{r_{21}^{p} - s}{r_{32}^{p} - s}\right) \tag{9}$$

$$s = 1 \cdot \mathrm{sgn}\left(\varepsilon_{32}/\varepsilon_{21}\right) \tag{10}$$

The extrapolated values are shown in Eq. (11):

$$\phi_{ext}^{21} = \left(r_{21}^{p}\phi_1 - \phi_2\right)/\left(r_{21}^{p} - 1\right) \tag{11}$$

The estimated relative error, denoted as e_a^{21}, the extrapolated relative error, denoted as e_{ext}^{21}, and the fine grid convergence index, denoted as GCI_{fine}^{21}, can be calculated using Eq. (12) to Eq. (14).

$$e_a^{21} = \left|\frac{\phi_1 - \phi_2}{\phi_1}\right| \tag{12}$$

$$e_{ext}^{21} = \left|\frac{\phi_{ext}^{12} - \phi_1}{\phi_{ext}^{12}}\right| \tag{13}$$

$$GCI_{fine}^{21} = \frac{1.25 e_a^{21}}{r_{21}^{p} - 1} \tag{14}$$

In this study, comparative analysis was conducted using three grids that varied in size. The outer domain of the most refined grid was set to a grid size of 50 mm, while the floors, facade, and circular openings of the building were set to a grid size of 0.5 mm, 0.5 mm, and 0.4 mm, respectively. The grid size of other parts of the building was adjusted to 1 mm, which leads to a total of 15,889,281 cells. Moreover, a coarser grid, based on the medium-sized grid, was developed, which doubled the grid size in the fluid domain and enlarged the details of the courtyard building in a similar way, thus resulting in 2,391,933 cells. Grid sensitivity was assessed by choosing the second floor at coordinates X = 135 mm, Z = 49 mm, and by increasing Y from 50 mm to 300 mm.

To observe the magnitude of wind velocity (m/s), a set of 26 points was deployed, whose readings at three different grid sizes are shown in Fig. 7 (a). The data shown in Table 1 emphasises points at Y = 70 mm, Y = 140 mm, and Y = 210 mm, with their grid convergence index reaching 1.646 %, 4.223 %, and 0.421 %, respectively. The medium mesh size was used for this study, considering its relatively limited error margin compared to the fine mesh. Meanwhile, computational cost was reduced significantly. Fig. 7 (b) shows the convergence index and discretisation error bars at all 26 points for the medium grid. The maximum GCI_{fine}^{21} was recorded at Y = 220 mm with a value of 5.56 %, which is considered acceptable. Additionally, the average GCI_{fine}^{21} at all 26 points was calculated to be 2.37 %, confirming that the medium mesh size is appropriate for simulation.

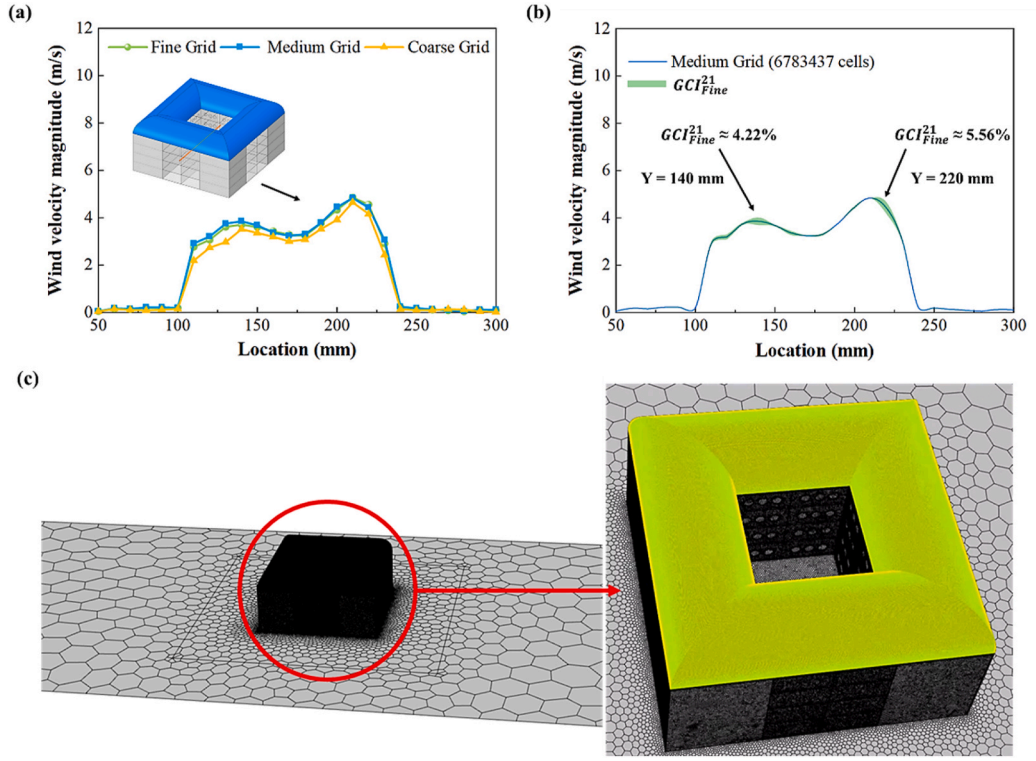

Fig. 7. (a) Simulation results of wind velocity magnitude along a horizontal centre line of the courtyard model at the height of 49 mm for the grid sensitivity analysis. (b) grid sensitivity analysis conducted using the GCI method. (c) polyhedral mesh around the courtyard building.

Table 1
Example of discretisation error computation employing the GCI method.

	Wind velocity magnitude (m/s) at Y = 70 mm	Wind velocity magnitude (m/s) at Y = 140 mm	Wind velocity magnitude (m/s) at Y = 210 mm
N1	15,889,281	15,889,281	15,889,281
N2	6,783,437	6,783,437	6,783,437
N3	2,391,933	2,391,933	2,391,933
r_{21}	1.328	1.328	1.328
r_{32}	1.415	1.415	1.415
ϕ_1	0.139	3.710	4.853
ϕ_2	0.146	3.851	4.836
ϕ_3	0.103	3.514	4.656
p	5.460	2.657	2.516
ϕ^{21}_{ext}	0.137	3.585	4.869
e^{21}_{a}	4.883 %	3.801 %	0.351 %
e^{21}_{ext}	1.335 %	3.497 %	0.336 %
GCI^{21}_{fine}	1.646 %	4.223 %	0.421 %

5. Results

5.1. Validation of the naturally ventilated courtyard model

The CFD simulations were developed to replicate the conditions of the wind tunnel experiments described in Refs. [43,44], as illustrated in Fig. 8a. The courtyard model followed the same 1:100 scale and multi-story layout used in the physical tests, ensuring consistency in geometry and boundary configuration for validation purposes.

In the experimental study, airflow rates through the model were not measured at individual surface points but instead derived from pressure drops across an orifice plate installed within one of the modular building components. This method allowed for indirect but accurate calculation of volumetric flow using calibrated differential pressure readings, ensuring minimal disruption to the flow field. Dynamic pressure was simultaneously measured at the top of the boundary layer (800 mm) using a pitot-static tube, which provided the reference velocity (V_{800}) needed for validation. Fig. 4 shows a schematic layout of the wind tunnel setup and representative

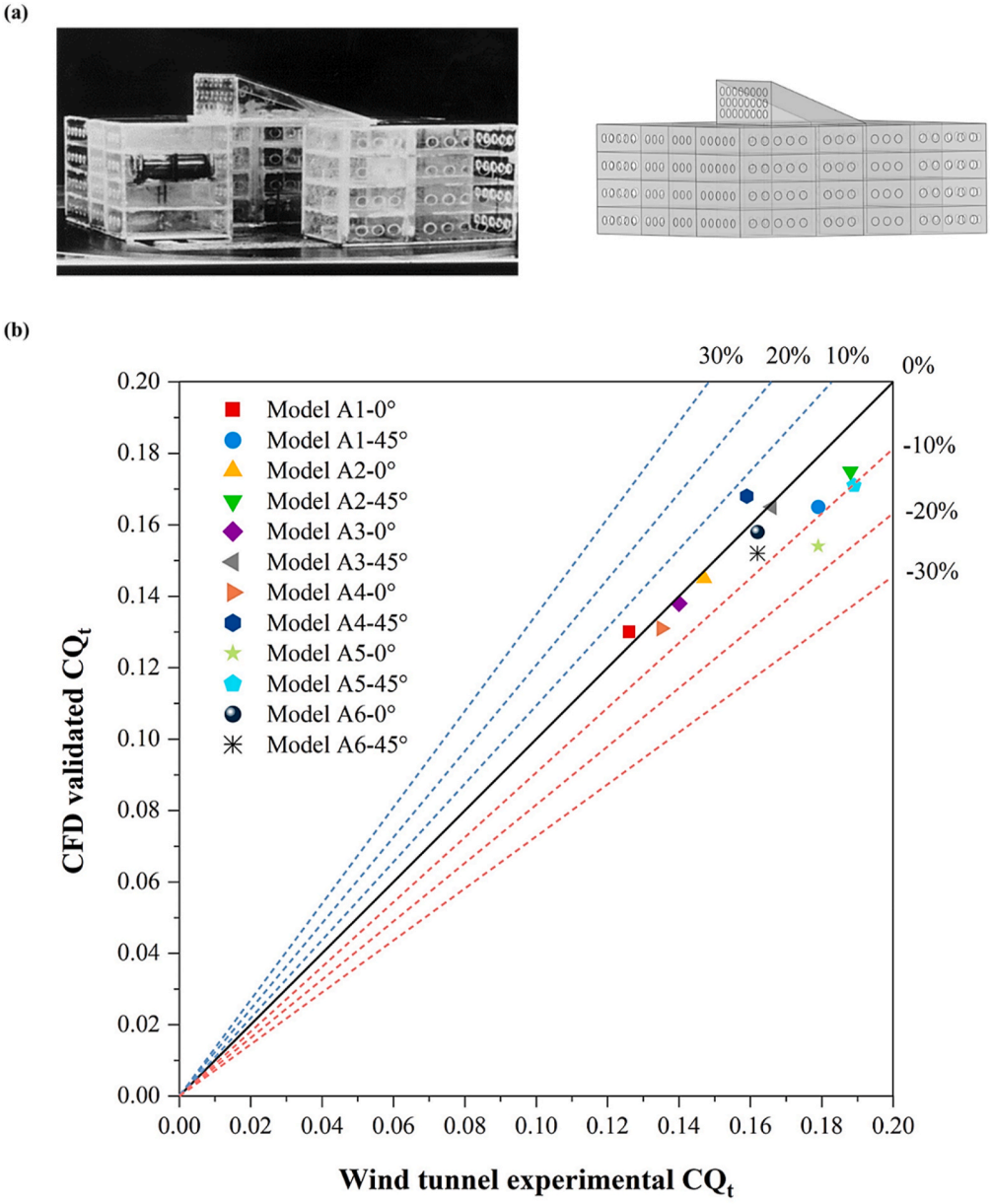

Fig. 8. (a) Comparison of the actual experimental model [44] and CFD numerical model. (b) deviation analysis for wind tunnel experiments and numerical simulations by using the *k*-omega Standard model in the courtyard and atriums.

measurement points. It should be noted that the illustration highlights only a subset of the full measurement configuration used in the actual wind tunnel experiment.

During the experimental process, measurement was performed for various building models, including a courtyard and multiple atrium structures, all of which were 339 mm in length, 339 mm in width, and 130 mm in height. Specifically, the atrium model with a roof at 22° had a height of 52 mm. In this study, six different isolated models were involved in CFD validation: Model A1 that represents a closed courtyard; Model A2 that represents an atrium devoid of roof openings; Models A3 and A5, both of which have roof openings on the windward and leeward sides, with a window-to-wall ratio of 11.4 %; and Models A4 and A6, each of which has a window-to-wall ratio of 30.4 %. Moreover, five commonly used RANS models were chosen: the *k*-epsilon Standard, *k*-epsilon RNG, *k*-epsilon Realisable, *k*-omega Standard, and *k*-omega SST. Considering courtyard architecture as the focus of this study, the courtyard model used for simulation was constructed by adapting Model A1. Through CFD modelling validation, all four models were assessed in terms of geometry, dimension, the working section of the wind tunnel, the window-to-wall ratio, and the boundary conditions. Each model was subjected to blowing by the wind at 0° and 45° to evaluate their effectiveness. Sharples and Bensalem used an orifice plate to measure

airflow rate in the model and introduced a novel dimensionless coefficient (CQ_t) into the experimental process. It was calculated using the following formula.

$$CQ_t = \frac{1}{N}\sum_{i=1}^{N}\frac{V_0}{V_{800}} \tag{15}$$

where V_0 represents the velocity at the opening *i*. As shown in Appendix Table A1 to Table A5, the RANS models, and especially the *k*-omega standard variant, are applicable to predict the pattern of wind distribution for the courtyard and atrium buildings. Fig. 8 (b) shows that the experimental and validation results (based on the *k*-omega standard model) are clearly consistent, with a greater level of similarity than 80 %. Notably, when the wind direction is 0°, the validation results of Model A1, Model A3, Model A4 and Model A6 are almost consistent with the experimental results. The errors are less than 5 %. It illustrates the high efficiency of CFD in accurately predicting the results of wind tunnel experiments and underscores the reliability and accuracy of the following simulation studies.

5.2. *Airflow in the single-sided ventilated courtyards with different shapes of roof*

In the flat-roof courtyard model (Fig. 9), airflow enters from the positive x-direction. The airflow impacts the windward face, where part of it moves upward toward the roof. The obstructive effect of the building, combined with the uneven distribution of wind pressure, forces the airflow upwards, thus creating an upward current along the external walls. A small vortex forms below the windward face due to boundary layer separation. As the air reaches the flat roof, it partially crosses the roof edge and flows downwards. On the leeward side of the building, a significant clockwise vortex is generated. Some of this vortex flows back over the roof, forming another clockwise vortex. This vortex redirects toward the courtyard after hitting the left facade. Part of this large vortex changes in direction upon contact with the left facade of the courtyard, directing the flow into the courtyard. Inside the courtyard, a counterclockwise vortex develops under the constraint of the surrounding walls, which promotes the influx of fresh air and thus improves the outcome of ventilation indoors.

Fig. 9 shows the wind speed distribution at Y = 137 mm in the baseline model. In the single-sided ventilated courtyard, the indoor wind speed stays at a relatively low level. Stronger airflow enters the top-floor windward rooms, indicating higher ventilation efficiency. On the leeward bottom floor, wind speeds exceed 0.1 m/s, showing continued airflow. Airflow in other rooms is lower but still

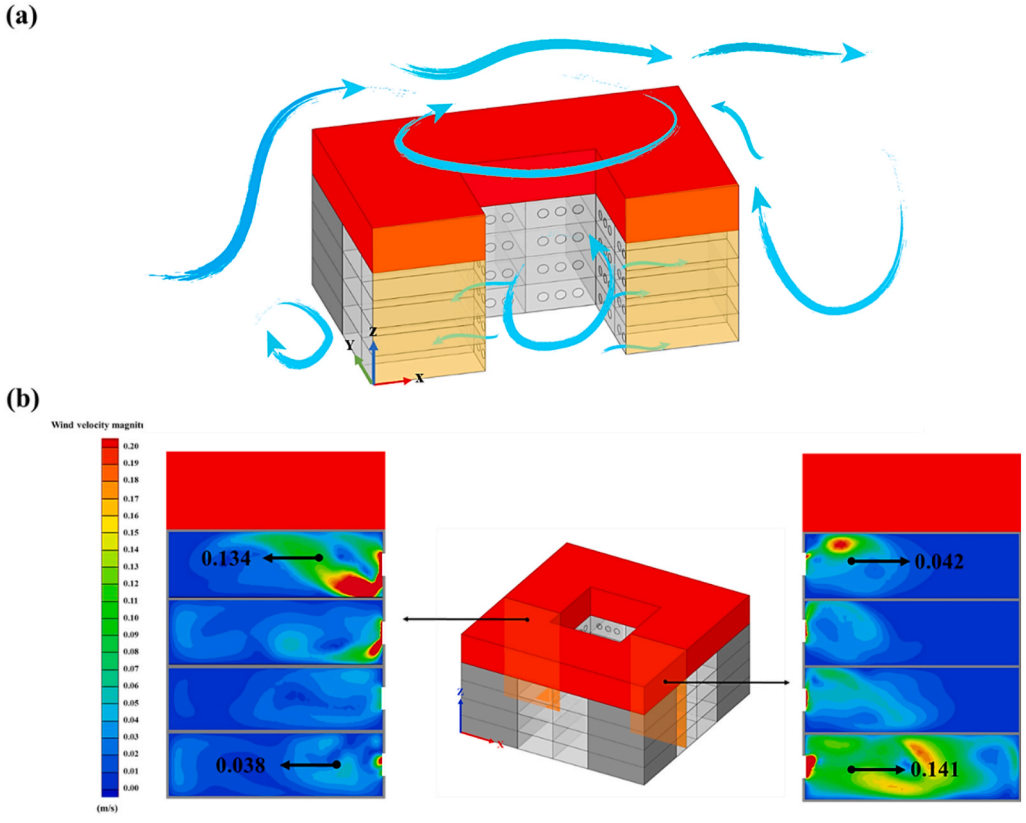

Fig. 9. Airflow movement patterns in the baseline flat-roof courtyard model and the indoor wind velocity magnitude contour at Y = 135 mm, with arrows representing the observed vectors.

present at the openings. The rooftop vortex induces a counterclockwise flow upon hitting the left courtyard wall. It first impacts the top-floor windward rooms, likely due to concentrated kinetic energy. Upon reaching the right facade, part of the airflow enters the leeward bottom rooms, while the rest moves upward.

Fig. 10 presents airflow patterns for ten roof styles, highlighting how roof geometry influences wind direction and velocity above the courtyard. Compared to the flat roof baseline (Fig. 10 a), other roofs primarily affect airflow above and beyond the leeward side. In the gambrel roof case (Fig. 10 d), wind slows along the shallow windward slope before accelerating upward. At the steeper lower slope, airflow forms tight streamlines and accelerates, especially near the roof edges where pressure-induced turbulence develops. As the flow passes the apex to the leeward side, roof-induced separation generates vortices along the right slope. This leads to a clockwise vortex forming above the courtyard.

In the dome roof case (Fig. 10 b), its streamlined design facilitates smooth airflow along the windward surface with minimal resistance. The curvature promotes flow adherence and reduces separation. This results in stable streamlines at the top. Unlike sharp-edged roofs, the dome induces fewer flow disturbances, minimising vortex formation. Downstream of the dome crest, separation induces a low-pressure zone. This promotes vortex formation at the roof base. Vortices propagate along the leeward edge, directing airflow into the courtyard zone. The dome's symmetry ensures balanced leeward vortex distribution, enhancing courtyard airflow. Fig. 10 (c)–(e), and (f) display the Chinese curved, mansard, and open gable roofs. Despite geometric differences, these roofs exhibit similar airflow behaviour. The incoming wind ascends along the windward slope, with streamlines rising toward the apex. Roof geometry and wind speed collectively shape the formation of leeward vortices, which direct airflow into or above the courtyard. The mansard roof, with dual slopes, intensifies vortex interaction at the fold. The Chinese curved roof reduces flow separation, producing smoother edge vortices, while the open gable roof induces sharp separation at the apex, generating focused vortex zones. While the vortex shapes vary slightly, all roofs share a consistent pattern of uplift, separation, and circulation.

Both the parapet and butterfly roofs (Fig. 10 (g) and (h)) feature pronounced indentations that promote vortex formation. In the parapet roof, raised edge walls create recessed zones that obstruct wind at the windward crest, triggering vortex development. The airflow continues along the top edge to the leeward side, where additional vortices emerge. The butterfly roof, with its V-shaped profile, channels wind toward the central trough, increasing flow velocity and intensifying vortex formation. The accelerated stream then rises along the roof slopes and separates near the apex, producing further downstream vortices. Fig. 10 (i) and (j) depict the shed and reverse shed roofs, emphasising their aerodynamic influence on courtyard airflow. In the shed roof configuration, the inclined plane channels wind upward, accelerating flow along the slope and generating strong vortices at the roof apex. In contrast, the reverse shed roof, featuring dual slopes and a vertical leeward face, directs airflow upward on both sides. However, the vertical surface inhibits flow entry into the courtyard, concentrating vortex formation above the roof rather than within the courtyard itself. Secondary vortices arise near the leeward edge due to intensified flow separation.

Fig. 11 compares five representative roof types: flat, dome, parapet, shed, and open gable. The velocity and pressure contours reveal distinct aerodynamic behaviours associated with each shape. For vertically oriented roofs such as the flat, parapet, and shed configurations, windward surfaces experience positive pressure exceeding 120 Pa, with respective external wind speeds of 3.1, 4.5, and 3.8 m/s. In contrast, inclined geometries like the open gable roof reduce windward pressure to around 48 Pa due to deflected upward flow. The dome roof exhibits superior aerodynamic efficiency—its curved profile reduces resistance, enabling wind acceleration up to 13.4 m/s along its surface. Over the roof apex, the pressure distribution varies significantly across roof types: negative pressures of −85 Pa (flat), −120 Pa (dome), and −53 Pa (gable) indicate stronger suction and vortex formation at the dome's leeward side. The parapet roof's recessed top intensifies low-pressure regions (below −100 Pa), triggering recirculation. Internally, the dome roof yields a peak airflow of 7.3 m/s, far surpassing other configurations, suggesting effective wind channelling into the building due to its symmetrical form.

5.3. *Effect of wind direction on airflow in single-sided ventilated courtyards with different roof shapes*

Fig. 12 (a) shows the airflow trajectories in courtyard buildings with a dome roof under three different wind directions: 0°, 30°, and 45°. At 0°, the wind approaches the courtyard perpendicularly from the west side, flowing smoothly along the dome surface due to its curvature. As the airflow passes over the roof and descends into the courtyard, symmetrical vortices are generated along the leeward edges. When the wind direction shifts to 30°, the inflow angle becomes more oblique, causing part of the airflow to be deflected along the southern façade before entering the courtyard. This angular incidence leads to asymmetric vortex formation and a more curved flow path over the roof. At 45°, the wind flows diagonally into the courtyard, striking both the eastern and northern façades simultaneously. This results in more direct airflow penetration into the courtyard area, forming a concentrated inflow path and strong rotational currents within the courtyard zone.

Fig. 12 (b) presents the average indoor wind velocity magnitudes for ten roof configurations under three wind directions (0°, 30°, and 45°). The data show a consistent performance ranking regardless of wind direction: the dome roof consistently yields the highest indoor airflow, while the parapet roof performs the weakest. Specifically, for the dome roof, the average wind velocity increases from 0.175 m/s at 0° to 0.325 m/s at 30°, and further to 0.491 m/s at 45°. In contrast, the parapet roof only reaches 0.025 m/s, 0.038 m/s, and 0.045 m/s under the same conditions, respectively. Across all roof types, wind velocity values at 30° are higher than those at 0°, and velocities at 45° are even greater. This trend suggests that oblique wind incidence enhances the interaction between the external airflow and the courtyard openings. For example, at 45°, the wind direction allows airflow to simultaneously engage with the eastern

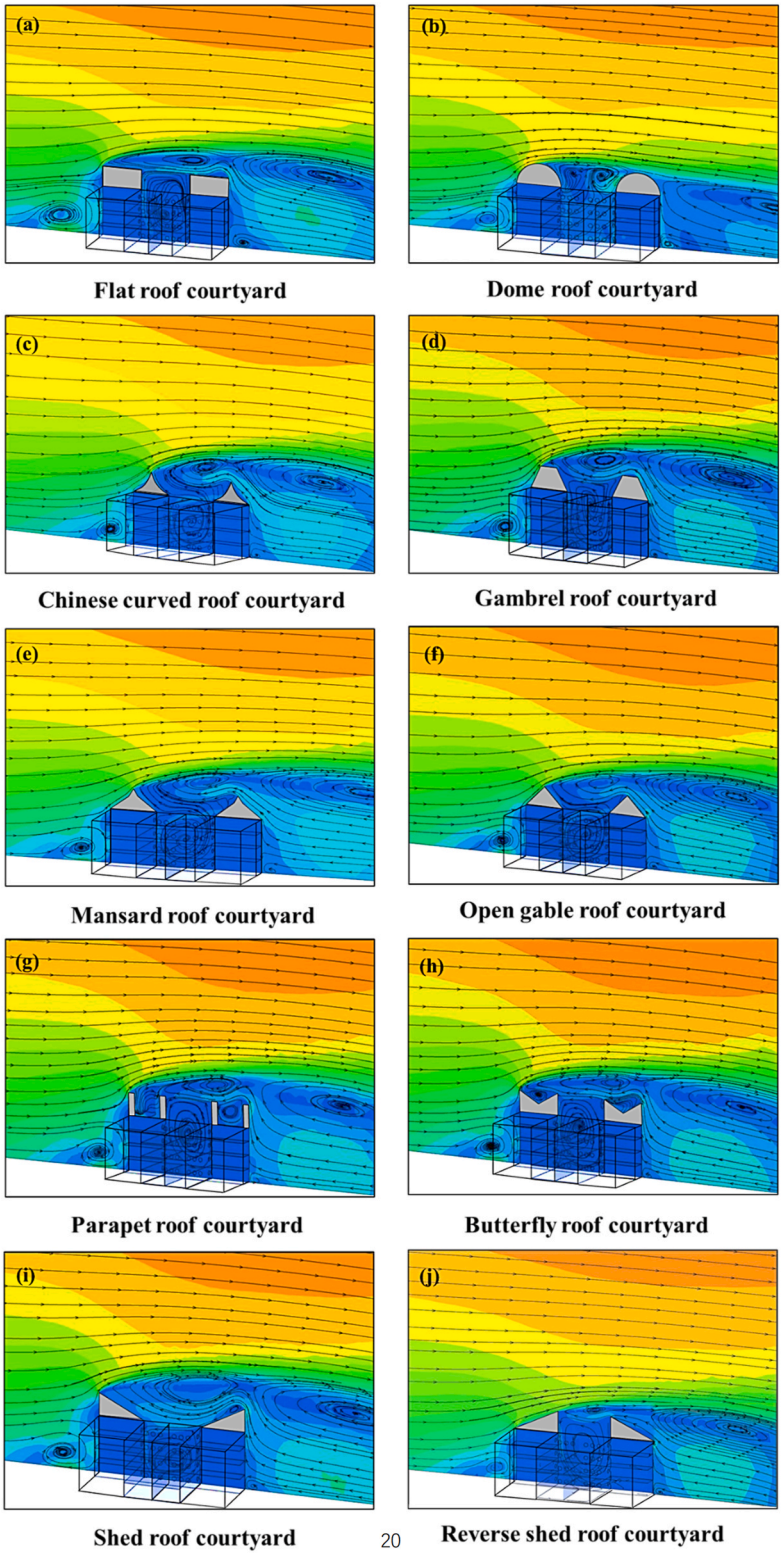

Fig. 10. Airflow at 0° movement patterns for ten different roof styles (a) flat roof courtyard. (b) dome roof courtyard. (c) Chinese curved roof courtyard. (d) gambrel roof courtyard. (e) mansard roof courtyard. (f) open gable roof courtyard. (g) parapet roof courtyard. (h) butterfly roof courtyard. (i) shed roof courtyard. (j) reverse shed roof courtyard.

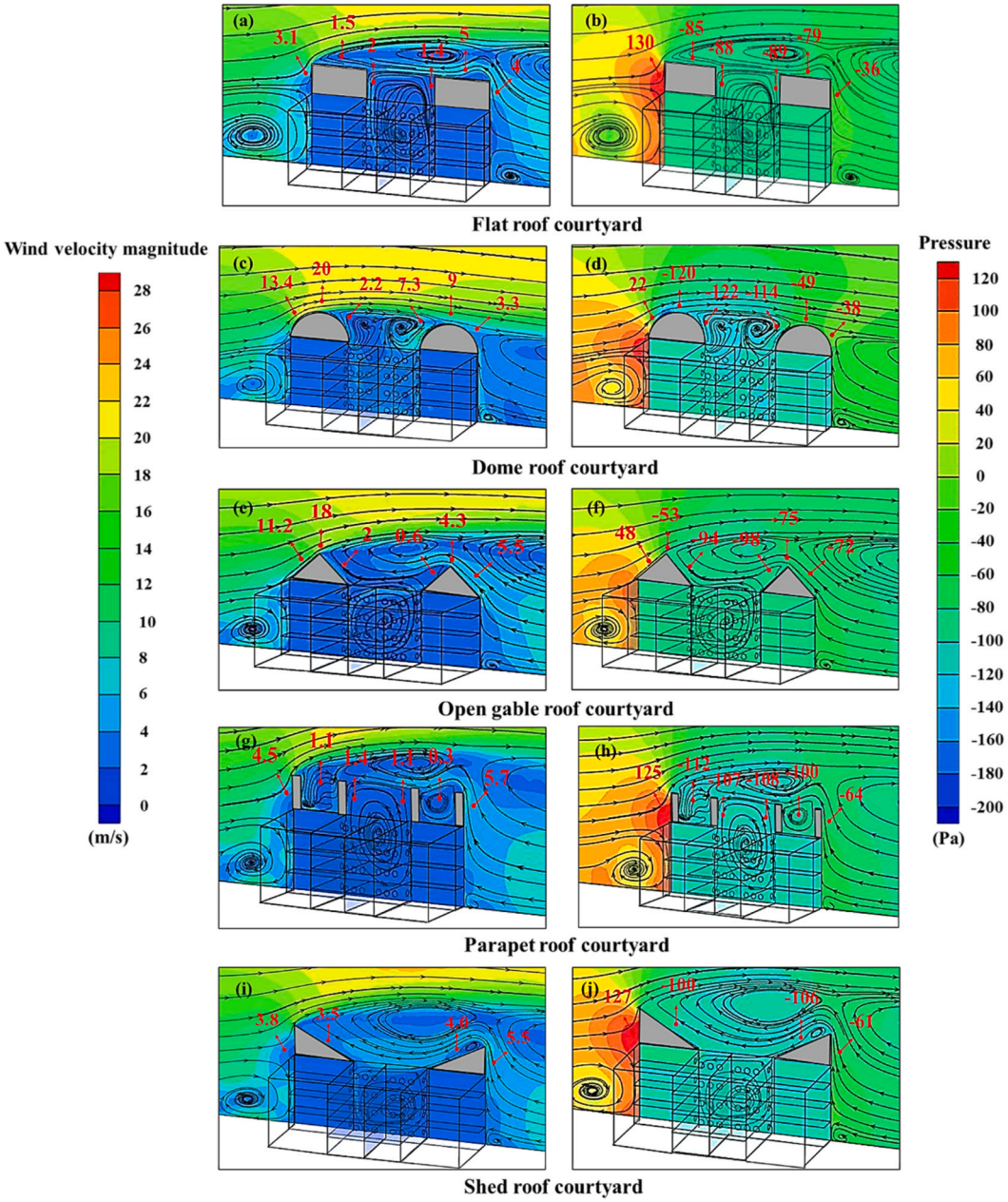

Fig. 11. Airflow at 0° movement patterns and pressure contours for five different roof styles with specific values (a) wind flow contour for the flat roof courtyard. (b) pressure contour for the flat roof courtyard. (c) wind flow contour for the dome roof courtyard. (d) pressure contour for the dome roof courtyard. (e) wind flow contour for the open gable roof courtyard. (f) pressure contour for the open gable roof courtyard. (g) wind flow contour for the parapet roof courtyard. (h) pressure contour for the parapet roof courtyard. (i) wind flow contour for the shed roof courtyard. (j) pressure contour for the shed roof courtyard.

and northern façades of the surrounding rooms, facilitating more efficient wind entry and circulation within the courtyard. The streamline contours on the second floor (Z = 81.25 mm), using the dome roof as a representative case, visually confirm this enhancement. Under 0° wind, airflow enters mainly through the windward side and circulates centrally. At 30°, diagonal flows begin to form, and at 45°, strong inflow jets emerge at two perpendicular façades, promoting more dynamic and widespread air movement throughout the interior spaces.

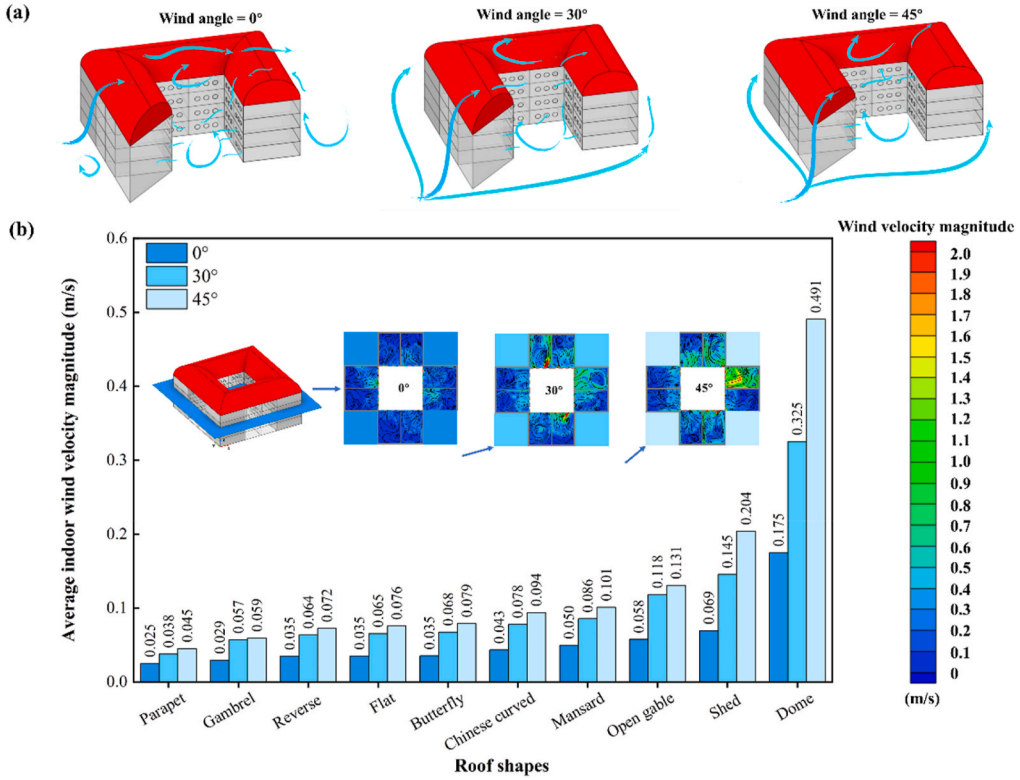

Fig. 12. (a) Airflow patterns of the courtyard with a dome roof under three wind directions (0°, 30°, and 45°). (b) comparison of average indoor wind velocity magnitude across ten roof shapes under three different wind directions, including contour visualization of velocity distribution for the dome roof case on the second floor (Z = 81.25 mm).

5.4. *Temperature distribution for the courtyard with different shapes of roof*

To evaluate how natural ventilation influences indoor cooling under different roof configurations, the CFD simulations maintained an outdoor temperature of 22 °C and applied a constant indoor heat flux of 5 W/m^2. Fig. 13 presents the indoor temperature contours (Y = 135 mm section) for four representative roof styles. The dome roof (Fig. 13 b) achieved the best cooling performance, with most

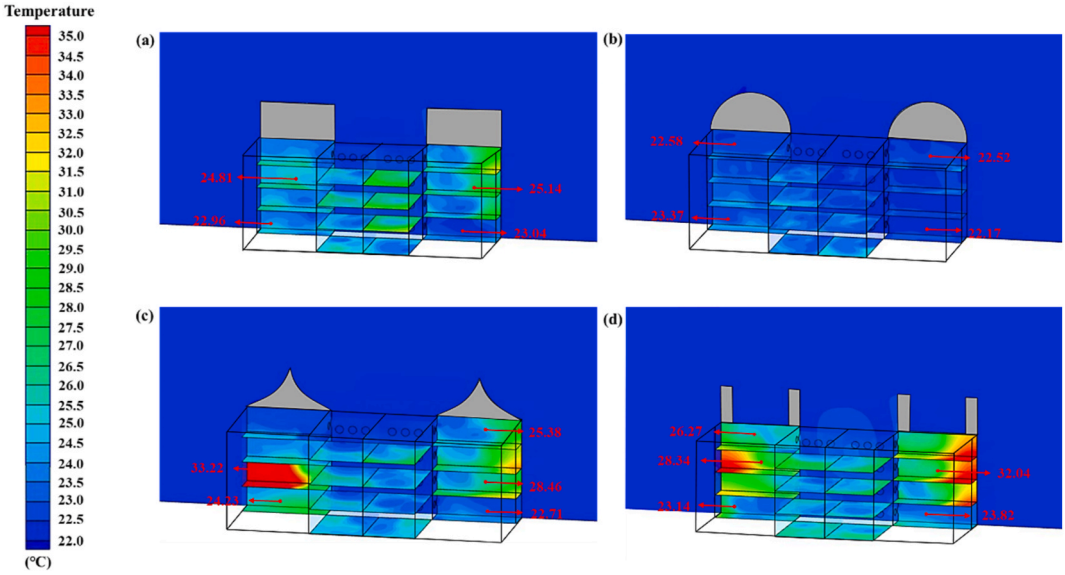

Fig. 13. Temperature contours in the cross-section at Y = 135 mm for the courtyard with four different roof styles at 0° (a) flat roof shape courtyard. (b) dome roof shape courtyard. (c) Chinese curved roof shape courtyard. (d) parapet roof shape courtyard.

rooms remaining below 24 °C. Particularly on the ground and first floors at the leeward side, temperature rise was minimal, suggesting efficient heat removal via stable airflow patterns. In contrast, the flat (Fig. 13 a) and Chinese curved (Fig. 13 c) roofs showed moderate cooling, with noticeable heat accumulation on the windward first-floor room in the latter, indicating local ventilation deficiencies. The parapet roof (Fig. 13 d) performed the worst, with all four rooms experiencing elevated temperatures, especially in deeper zones. This suggests inadequate airflow penetration and weak convective heat dissipation, despite the presence of external wind.

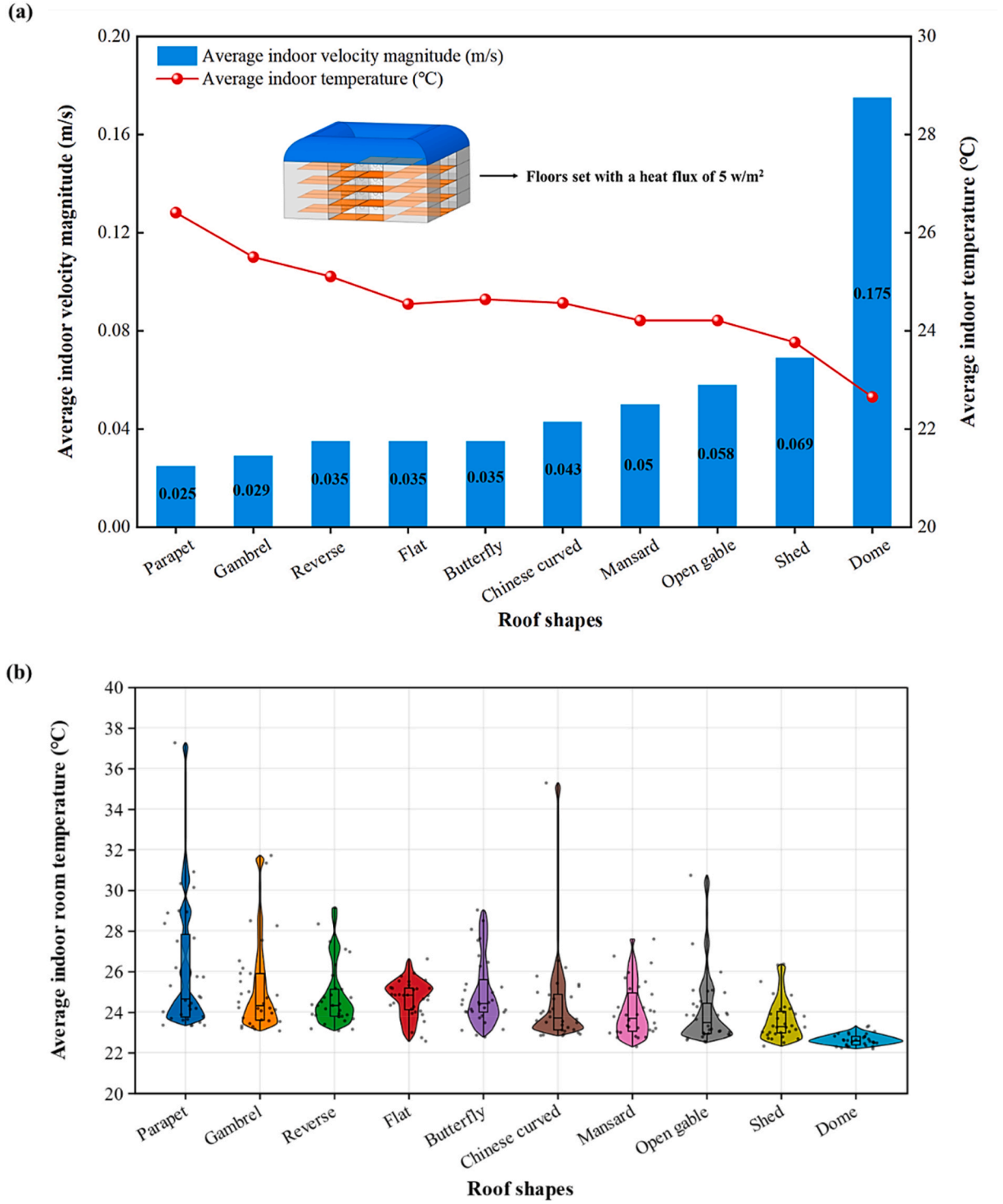

Fig. 14. (a) Comparison of average indoor wind velocity magnitude at 0° and average temperature for courtyard buildings with ten different roof styles. (b) distribution of average temperatures across 32 test rooms in courtyard buildings with ten roof styles.

Fig. 14 (a) shows the impact of 10 roof styles on average indoor temperature and wind speed in a single-sided ventilated courtyard. The dome roof performs best, achieving the highest wind speed (0.175 m/s) and lowest temperature (22.65 °C), while the parapet roof performs the worst, with the lowest wind speed (0.025 m/s) and highest temperature (26.41 °C). Notably, the dome roof's wind speed is seven times that of the parapet, with temperatures 14.23 % lower, demonstrating its superior cooling effect. The shed roof ranks second, reducing temperature by 2.65 °C compared to the parapet. Courtyards with indented designs, like the butterfly roof, show improved cooling compared to the parapet, with the butterfly roof's temperature 1.77 °C lower. The open gable roof leads to airflow-style designs, while the shed roof outperforms the reverse shed in ventilation and cooling. Overall, a higher wind speed generally correlates with lower indoor temperatures, highlighting the effectiveness of ventilation in cooling. Although the overall range of airflow velocity and temperature variation appears relatively modest across some of the roof types, these differences arise under identical boundary and thermal conditions. This reflects the sensitive influence of roof geometry on indoor thermal performance, where even subtle variations in airflow pattern can lead to measurable differences in passive cooling effectiveness.

Fig. 14 (b) compares average indoor temperatures and their variability across 32 rooms under ten roof configurations. The dome roof achieved the lowest and most stable thermal environment, with an average temperature of 22.61 °C and a standard deviation of 0.30, reflecting consistent heat removal. In contrast, the parapet roof exhibited the highest average temperature (26.01 °C) and the greatest variation (standard deviation of 3.14), indicating poor thermal regulation likely due to inadequate airflow circulation. The Chinese curved roof maintained a moderate average (24.37 °C) but occasionally reached higher extremes, suggesting partial ventilation inefficiencies. Roofs such as the shed, reverse shed, mansard, and butterfly provided relatively balanced performance, offering controlled indoor temperature fluctuations within acceptable ranges.

5.5. Analysis of the relationship between courtyard wind dynamics and indoor airflow enhancement

As shown in Fig. 15, the relationship between roof shape and the impact of courtyard indoor wind speed is shown. The dome roof achieves the highest indoor wind speed (0.175 m/s) and courtyard wind speed (3.429 m/s), demonstrating superior airflow into indoor spaces. In contrast, the parapet roof has the lowest indoor (0.0250 m/s) and courtyard (0.756 m/s) wind speeds, reflecting poor ventilation. The open gable roof shows moderate results, with indoor and courtyard speeds of 0.058 m/s and 1.219 m/s, respectively, indicating satisfactory ventilation. The shed roof also enhances indoor ventilation, reaching 0.070 m/s at a courtyard speed of 1.291 m/s. Roofs like the butterfly, flat, and reverse shed achieve similar indoor wind speeds, suggesting moderate ventilation at comparable courtyard wind speeds. While courtyard wind speeds differ slightly among these styles (all below 1.3 m/s except for the dome), the dome's structure directs airflow more effectively, achieving 2.5 times the indoor speed of the shed roof. The data also shows a strong positive correlation (about 0.99) between courtyard and indoor wind speeds, emphasising the role of courtyard design in supporting natural ventilation indoors. Despite the relatively small variation in courtyard wind speeds among most non-curved roof styles (generally below 1.3 m/s), their influence on indoor airflow remains evident. This highlights the sensitivity of indoor ventilation performance to courtyard wind conditions. The strong linear relationship observed between courtyard and indoor wind speeds is primarily governed by the turbulent flow patterns induced by different roof geometries. Each roof shape alters the aerodynamic behaviour above the building, resulting in variations in airflow separation, reattachment, and vortex formation. These turbulent characteristics directly influence both the volume and velocity of air entering the courtyard. For instance, streamlined roof forms such as dome or shed roofs promote smoother airflow over the windward side and more intense vortex formation on the leeward side, which accelerates the inflow of air into the courtyard. Once the air enters the courtyard, it remains in a turbulent state and is redistributed into adjacent indoor rooms through façade openings. Consequently, the greater the courtyard wind velocity, the more air can be driven into the interior spaces, enhancing natural ventilation. However, since different roofs regulate the airflow entering the courtyard to varying degrees, the resulting indoor airflow also varies accordingly. This explains why courtyard wind conditions, shaped by roof-induced turbulence, play a critical role in determining the effectiveness of indoor ventilation.

5.6. Analysis of the relationship between courtyard inflow air volume and indoor wind speed

Fig. 16 examines the impact of roof structures on indoor wind speed and airflow volume. The parapet roof shows the lowest ventilative cooling efficiency, with an indoor wind speed of 0.025 m/s and a volumetric flow rate of 4.38 x 10^{-4} m^3/s. The butterfly and reverse roofs perform moderately, with wind speeds between 0.035 and 0.035 m/s and flow rates near 5 x 10^{-4} m^3/s, indicating stable airflow. The open gable and shed roofs perform better, achieving 0.070 m/s and a flow rate of 1.04×10^{-4} m^3/s. The dome roof excels, with the highest indoor wind speed (0.175 m/s) and volumetric flow rate (2.17×10^{-4} m^3/s), providing 2.5 times the wind speed and 2.09 times the flow rate of the shed roof, highlighting its aerodynamics. Butterfly, flat, and reverse roofs exhibit similar indoor wind speeds, but flat and reverse roofs slightly outperform in volumetric flow, likely due to structural factors. Fig. 16 (b) shows a strong correlation ($R \approx 0.995$) between volumetric flow rate and indoor wind speed. The linear relationship observed between the volumetric flow rate of air entering the interior and the average indoor wind speed can be attributed to the aerodynamic influence of roof geometry on external and internal airflow paths. Roofs with streamlined shapes, such as the dome and shed, generate favourable pressure differentials that facilitate the entry of external air through the window openings. These geometries reduce flow separation and enhance suction on the leeward side, resulting in increased airflow penetration into the courtyard and subsequently into the rooms. Once the air enters the building, the greater the incoming volumetric flow, the more likely it is to form meaningful and sustained airflow paths within the interior space, thereby raising indoor wind velocity. In contrast, obstructive roof designs such as parapet roofs hinder the inflow of air due to reduced pressure gradients and turbulence stagnation near the openings, which limits both

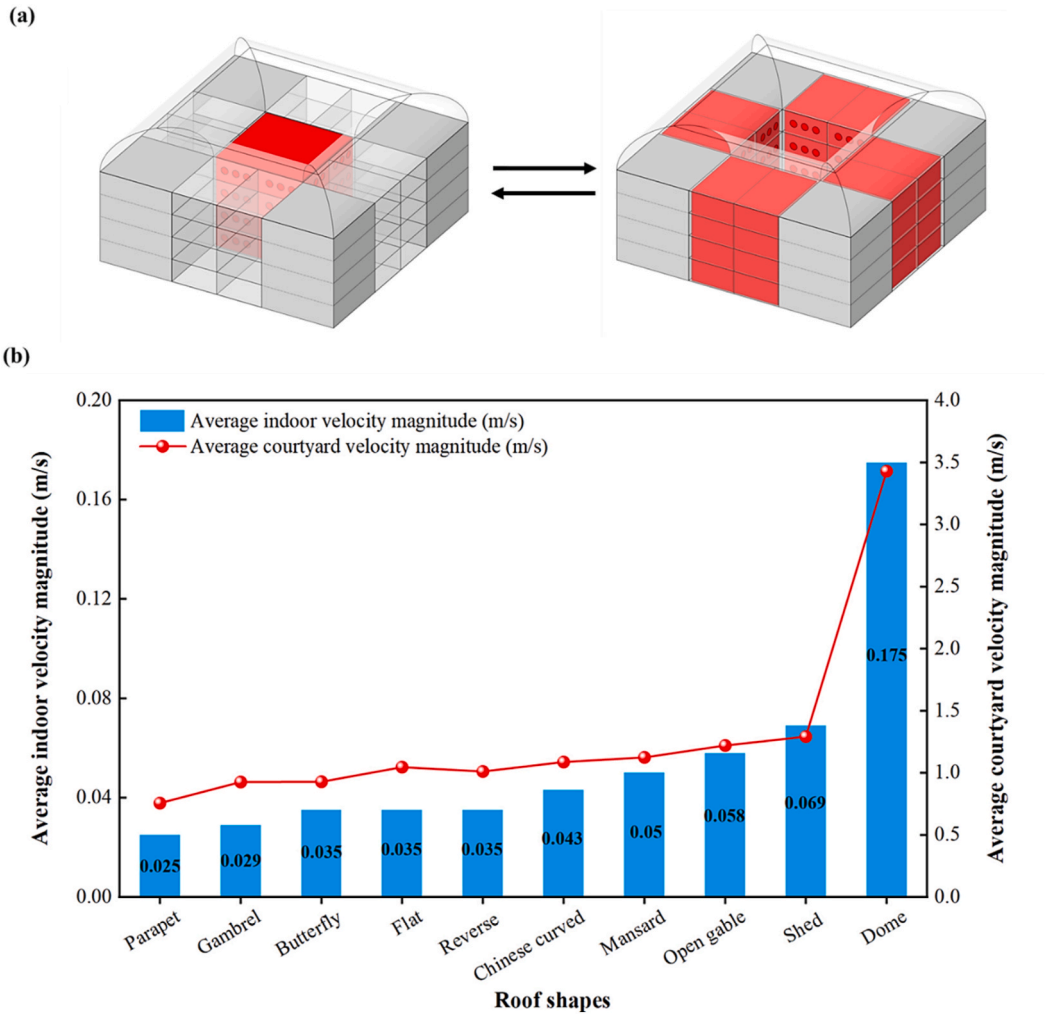

Fig. 15. (a) Investigation of the relationship between average wind velocity magnitudes at 0° in the courtyard and indoors. (b) comparison of average courtyard wind velocity magnitudes with indoor average wind velocities for courtyard buildings with 10 different roof styles.

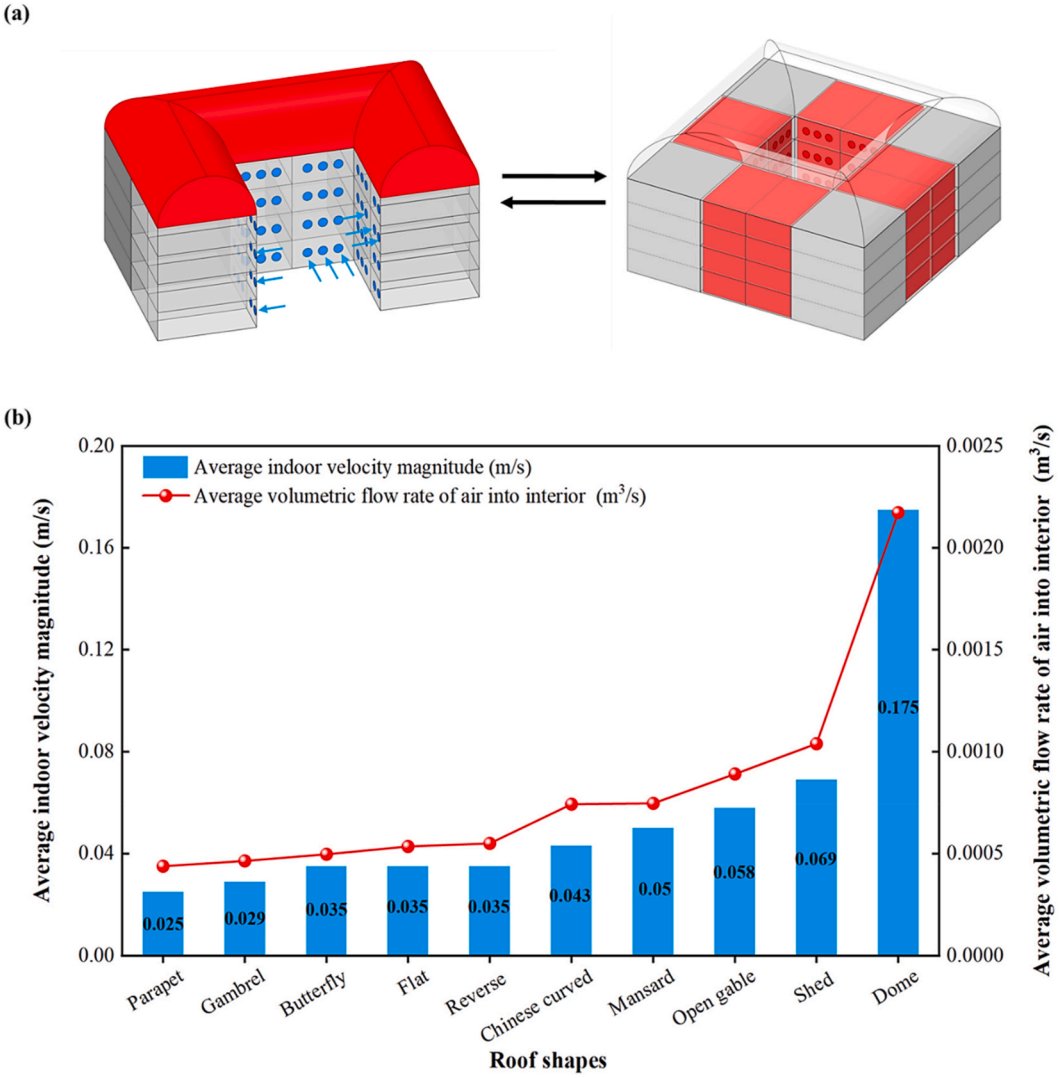

Fig. 16. (a) Exploration of the relationship between the volumetric flow rate of air entering indoors and average indoor wind velocity magnitude at 0°. (b) Comparison of indoor average wind velocity magnitudes and the volumetric flow rate of air entering indoors for courtyard buildings with 10 different roof styles.

airflow volume and internal wind speed. This demonstrates how roof-induced variations in courtyard wind dynamics directly modulate the driving force for indoor ventilation.

6. Discussion

In this section, the results of CFD simulations are compared with the previous relevant studies. Additionally, the potential areas of improvement are identified in this research.

6.1. Comparison with other studies

To deepen the discussion and contextualise our findings within the existing body of literature, this study highlights how roof geometry significantly influences the wind environment and natural ventilation performance in courtyard buildings. By analysing ten distinct roof styles, we observed that variations in roof shape alter the formation of recirculation zones, the reattachment length of airflow, and the position of shear layers above the courtyard. These aerodynamic differences directly affect courtyard airflow and subsequently influence indoor ventilation. This aligns with Prakash's study [38], which similarly reported that roof geometry plays a critical role in modifying airflow patterns within courtyard buildings.

Furthermore, our results show that certain roof shapes can enhance negative pressure zones within the courtyard, thereby

promoting wind-driven ventilation. For instance, roofs with streamlined or upward-sloping surfaces, such as dome and shed styles, were found to facilitate air inflow into indoor spaces. This observation is consistent with Peren et al. [36], who demonstrated that straight and convex roof forms can enhance negative pressure on the leeward side, improving cross-ventilation efficiency.

In particular, the dome roof stands out for its aerodynamic advantage. Our study confirms that dome-shaped roofs improve both courtyard and indoor airflow and support efficient thermal dissipation. This complements the findings of Esfeh et al. [57], through experimental and numerical analyses, emphasised that semi-cylindrical roofs improve ventilation performance, particularly when wind approaches perpendicularly (e.g., at 0° incidence). Their study also noted the role of roof height in sustaining internal airflow circulation and highlighted cost-effectiveness compared to alternative strategies such as wind-catchers. Asfour and Gadi [35] further reinforce this view by demonstrating that dome and vaulted roofs improve upstream and central airflow regions by redirecting wind through rooftop openings, offering greater efficiency than wall-based openings.

Compared to Prakash's work [38], which examined seven roof shapes, including flat, pitched, curved, and hybrid types. We included a wider variety of roof geometries, including butterfly and reverse shed styles. While Prakash found that pitched and curved-inward roofs were among the most effective, our study extends this conclusion by showing that dome roofs produce the best overall performance, while parapet roofs result in the weakest ventilation. This discrepancy may stem from differences in courtyard structure and model setup across studies. Importantly, our findings also indicate that roof geometry not only affects ventilation but also enhances indoor heat dissipation, a claim supported in Prakash's study [38], which observed improved indoor thermal comfort with changes in roof configuration.

Together, these comparisons underscore that our findings are consistent with, and extend beyond, current research on roof aerodynamics in courtyard environments. By incorporating a broader range of roof styles and explicitly linking airflow patterns with thermal performance, our study provides additional evidence on the critical role of roof geometry in shaping indoor environmental quality in passive building designs.

6.2. Limitations and recommendations for future work

This study primarily investigates how different roof styles influence the wind and thermal environment in single-sided ventilated courtyard buildings. However, it does not explore the specific effects of roof height or slope, such as the radius of curvature in dome roofs or the inclination angle in pitched roofs. Previous research by Zobaied et al. [37] has shown that steeper roof slopes can increase airflow velocity near window and roof openings by altering the pressure distribution. These findings suggest that future studies should systematically examine how variations in roof slope and height affect airflow characteristics and ventilation performance.

In addition, the current study is based on wind tunnel experiments using scaled courtyard models. While these models allow for controlled validation, they may not fully reflect the boundary conditions and physical complexity of actual buildings. Therefore, future research should consider applying the findings to full-scale simulations and complementing them with field measurements in real courtyard buildings.

Finally, for the CFD validation and simulation, this study adopts the RANS approach using the standard k-omega model. This choice balances accuracy and computational efficiency, particularly given the need to compare multiple design scenarios. However, more advanced turbulence models such as large eddy simulation (LES) have demonstrated higher accuracy in capturing flow separation and vortex behaviour in complex geometries. Future studies could adopt LES methods to gain deeper insights into the detailed flow structures affected by specific roof features.

7. Conclusion

This study investigates how ten common roof styles influence the wind and thermal performance of single-sided ventilated courtyard buildings through validated CFD simulations. The results reveal that roof geometry significantly affects airflow patterns above the roof, the formation of recirculation zones, and the negative pressure areas within the building, which collectively shape natural ventilation performance.

Key findings include:

1. Roof style has a clear impact on indoor airflow. Dome roofs demonstrated the most efficient ventilation, generating the highest indoor wind speed (0.175 m/s), while parapet roofs were the least effective (0.025 m/s). The streamlined form of the dome enhances flow attachment and reduces turbulence, improving ventilation outcomes.
2. These patterns remain consistent across varying wind directions (0°, 30°, and 45°). The aerodynamic advantage of dome and shed roofs was maintained, confirming the robustness of the results.
3. Indoor temperature was closely linked to ventilation performance. Courtyards with higher indoor airflow achieved better heat dissipation. The dome roof reduced indoor temperature to 22.61 °C, compared to 24.45 °C under a parapet roof.
4. Strong linear correlations were found between indoor airflow, courtyard wind speed, and volumetric inflow. These results emphasise the importance of roof design in enhancing passive cooling and ventilation efficiency.

These findings are particularly relevant to hot regions and high-density urban areas, where mechanical cooling systems are energy-intensive and natural ventilation is both desirable and necessary. In compact cities where buildings have limited cross-ventilation potential, single-sided ventilation via courtyards becomes crucial. In such scenarios, dome and shed roofs can be strategically employed to optimise airflow into rooms facing internal courtyards, thereby improving ventilation and indoor comfort, reducing

reliance on air conditioning, and supporting the development of low-carbon and climate-adaptive buildings. However, in colder or extremely humid climates, the significant airflow enhancement provided by dome or shed roofs could increase heat losses or introduce moisture management issues, potentially reducing energy efficiency and compromising indoor comfort. Therefore, this study provides both a practical design reference and a climate-sensitive perspective for architects and engineers working toward more sustainable and zero-carbon courtyard buildings.

CRediT authorship contribution statement

Hao Sun: Writing – review & editing, Writing – original draft, Visualization, Validation, Software, Resources, Methodology, Investigation, Formal analysis, Data curation, Conceptualization. **Rafik Bensalem:** Writing – original draft, Validation, Supervision, Methodology, Investigation, Conceptualization. **Abdullah Dik:** Writing – review & editing, Writing – original draft, Validation, Methodology, Investigation, Formal analysis, Data curation. **Zhu Tao:** Writing – original draft, Software, Resources, Methodology, Formal analysis, Data curation. **Zhe Wang:** Writing – original draft, Visualization, Validation, Methodology, Investigation. **Carlos Jimenez-Bescos:** Writing – review & editing, Writing – original draft, Supervision. **John Kaiser Calautit:** Writing – review & editing, Writing – original draft, Visualization, Validation, Supervision, Software, Project administration, Methodology, Investigation, Formal analysis, Data curation, Conceptualization.

Declaration of competing interest

The authors declare that they have no known competing financial interests or personal relationships that could have appeared to influence the work reported in this paper.

Appendix

Table A.1
Velocity coefficient CQt validation results for the courtyard and atriums numerical simulation by using *k*-epsilon Standard model.

Model	Models	Wind direction (°)	Experimental CQ_t	*k*-epsilon Standard CQ_t	Error (%)
Model A1	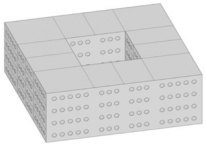	0	0.126	0.135	7.18
		45	0.179	0.147	17.87
Model A2	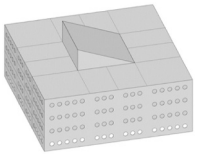	0	0.147	0.140	4.76
		45	0.188	0.164	12.53
Model A3	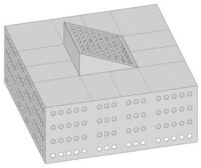	0	0.140	0.141	1.03
		45	0.166	0.141	15.01
Model A4	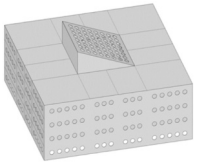	0	0.135	0.139	2.96
		45	0.159	0.142	10.69

(*continued on next page*)

Table A.1 (*continued*)

Model	Models	Wind direction (°)	Experimental CQ_t	*k*-epsilon Standard CQ_t	Error (%)
Model A5	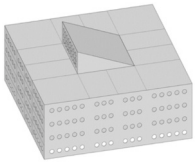	0	0.179	0.148	17.32
		45	0.189	0.167	11.64
Model A6	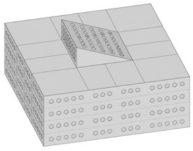	0	0.162	0.138	14.81
		45	0.162	0.137	15.43

Table A.2
Velocity coefficient CQt validation results for the courtyard and atriums numerical simulation by using *k*-epsilon RNG model.

Model	Models	Wind direction (°)	Experimental CQ_t	*k*-epsilon RNG CQ_t	Error (%)
Model A1	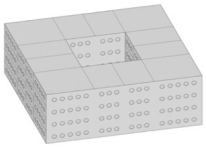	0	0.126	0.119	5.28
		45	0.179	0.160	10.61
Model A2	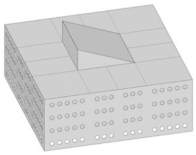	0	0.147	0.145	1.26
		45	0.188	0.172	8.53
Model A3	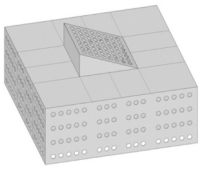	0	0.140	0.130	7.19
		45	0.166	0.160	3.73
Model A4	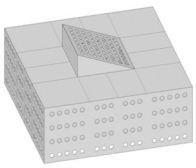	0	0.135	0.147	8.89
		45	0.159	0.164	3.14
Model A5	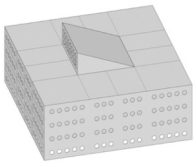	0	0.179	0.141	21.22
		45	0.189	0.171	9.52

(*continued on next page*)

Table A.2 (*continued*)

Model	Models	Wind direction (°)	Experimental CQ_t	*k*-epsilon RNG CQ_t	Error (%)
Model A6	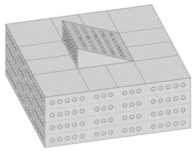	0	0.162	0.140	13.58
		45	0.162	0.155	4.32

Table A.3
Velocity coefficient CQt validation results for the courtyard and atriums numerical simulation by using *k*-epsilon Realisable model.

Model	Models	Wind direction (°)	Experimental CQ_t	*k*-epsilon Relizable CQ_t	Error (%)
Model A1	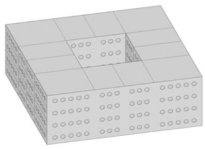	0	0.126	0.129	2.33
		45	0.179	0.161	11.18
Model A2	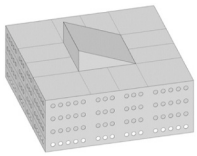	0	0.147	0.142	3.52
		45	0.188	0.168	11.90
Model A3	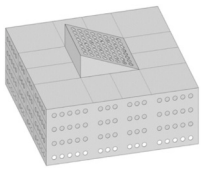	0	0.140	0.140	0
		45	0.166	0.145	14.48
Model A4	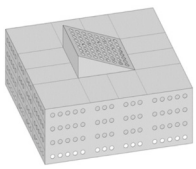	0	0.135	0.140	3.70
		45	0.159	0.154	3.14
Model A5	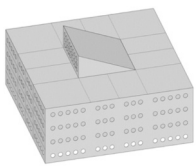	0	0.179	0.151	18.54
		45	0.189	0.171	9.52
Model A6	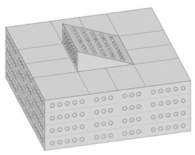	0	0.162	0.138	14.81
		45	0.162	0.137	15.43

Table A.4
Velocity coefficient CQt validation results for the courtyard and atriums numerical simulation by using *k*-omega Standard model.

Model	Models	Wind direction (°)	Experimental CQ_t	*k*-omega Standard CQ_t	Error (%)
Model A1	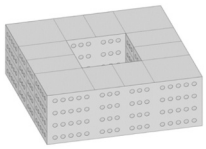	0	0.126	0.130	3.36
		45	0.179	0.165	7.82
Model A2	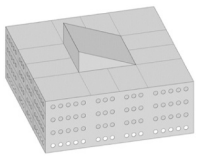	0	0.147	0.145	1.26
		45	0.188	0.175	6.73
Model A3	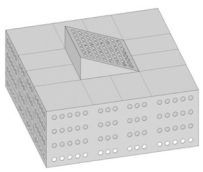	0	0.140	0.138	1.62
		45	0.166	0.165	0.06
Model A4	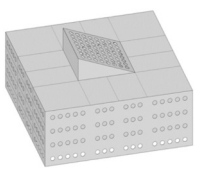	0	0.135	0.131	2.96
		45	0.159	0.168	5.66
Model A5	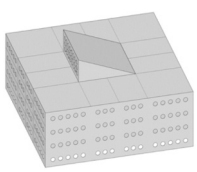	0	0.179	0.154	16.23
		45	0.189	0.171	9.52
Model A6	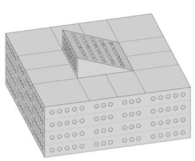	0	0.162	0.158	2.47
		45	0.162	0.152	6.71

Table A.5
Velocity coefficient CQt validation results for the courtyard and atriums numerical simulation by using *k*-omega SST model.

Model	Models	Wind direction (°)	Experimental CQ_t	*k*-omega SST CQ_t	Error (%)
Model A1	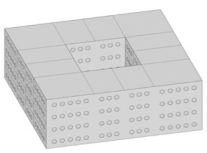	0	0.126	0.126	0
		45	0.179	0.162	9.50

(*continued on next page*)

Table A.5 (*continued*)

Model	Models	Wind direction (°)	Experimental CQ_t	*k*-omega SST CQ_t	Error (%)
Model A2	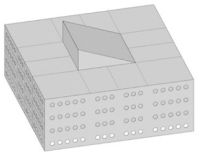	0	0.147	0.145	1.26
		45	0.188	0.174	7.30
Model A3	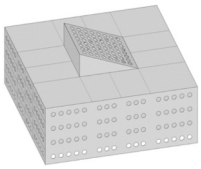	0	0.140	0.137	1.62
		45	0.166	0.157	5.65
Model A4	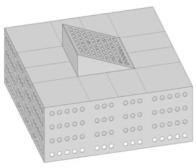	0	0.135	0.142	5.19
		45	0.159	0.173	8.81
Model A5	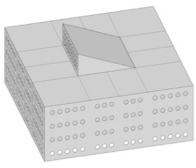	0	0.179	0.148	17.32
		45	0.189	0.174	7.93
Model A6	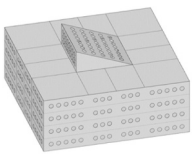	0	0.162	0.140	13.58
		45	0.162	0.150	7.50

Data availability

Data will be made available on request.

References

[1] S. Gunasagaran, B.T. Shiowee, T. Mari, S. Srirangam, V.F.P. Ng, Revisiting the courtyard as lived heritage and social space, J. Eng. Sci. Technol. 17 (2022) 74–89.

[2] P. Saadatjoo, P. Badamchizadeh, M. Mahdavinejad, Towards the new generation of courtyard buildings as a healthy living concept for post-pandemic era, Sustain. Cities Soc. 97 (2023) 104726, https://doi.org/10.1016/j.scs.2023.104726.

[3] A. Aldawoud, Thermal performance of courtyard buildings, Energy Build. 40 (2008) 906–910, https://doi.org/10.1016/j.enbuild.2007.07.007.

[4] L. Yang, M. Ye, B.-J. He, CFD simulation research on residential indoor air quality, Sci. Total Environ. 472 (2014) 1137–1144, https://doi.org/10.1016/j.scitotenv.2013.11.118.

[5] H. Sun, C. Jimenez-Bescos, M. Mohammadi, F. Zhong, J.K. Calautit, Numerical investigation of the influence of vegetation on the aero-thermal performance of buildings with courtyards in hot climates, Energies 14 (2021) 5388, https://doi.org/10.3390/en14175388.

[6] I. Rajapaksha, H. Nagai, M. Okumiya, A ventilated courtyard as a passive cooling strategy in the warm humid tropics, Renew. Energy 28 (2003) 1755–1778, https://doi.org/10.1016/S0960-1481(03)00012-0.

[7] V. Ok, E. Yasa, M. Özgunler, An experimental study of the effects of surface openings on air flow caused by wind in courtyard buildings, Archit. Sci. Rev. 51 (2008) 263–268, https://doi.org/10.3763/asre.2008.5131.

[8] Z. Zamani, S. Heidari, P. Hanachi, Reviewing the thermal and microclimatic function of courtyards, Renew. Sustain. Energy Rev. 93 (2018) 580–595, https://doi.org/10.1016/j.rser.2018.05.055.

[9] M. Li, Y. Jin, J. Guo, Dynamic characteristics and adaptive design methods of enclosed courtyard: a case study of a single-story courtyard dwelling in China, Build. Environ. 223 (2022) 109445, https://doi.org/10.1016/j.buildenv.2022.109445.

[10] Y. Gao, R. Yao, B. Li, E. Turkbeyler, Q. Luo, A. Short, Field studies on the effect of built forms on urban wind environments, Renew. Energy 46 (2012) 148–154, https://doi.org/10.1016/j.renene.2012.03.005.
[11] E. Jamei, P. Rajagopalan, M. Seyedmahmoudian, Y. Jamei, Review on the impact of urban geometry and pedestrian level greening on outdoor thermal comfort, Renew. Sustain. Energy Rev. 54 (2016) 1002–1017, https://doi.org/10.1016/j.rser.2015.10.104.
[12] Y. Takano, P. Moonen, On the influence of roof shape on flow and dispersion in an urban street canyon, J. Wind Eng. Ind. Aerod. 123 (2013) 107–120, https://doi.org/10.1016/j.jweia.2013.10.006.
[13] J. Singh, A.K. Roy, Effects of roof slope and wind direction on wind pressure distribution on the roof of a square plan pyramidal low-rise building using CFD simulation, Int. J. Adv. Struct. Eng. 11 (2019) 231–254, https://doi.org/10.1007/s40091-019-0227-3.
[14] W. Shan, Y. Tamura, Q. Yang, B. Li, Effects of curved slopes, high ridges and double eaves on wind pressures on traditional Chinese hip roofs, J. Wind Eng. Ind. Aerod. 183 (2018) 68–87, https://doi.org/10.1016/j.jweia.2018.10.010.
[15] I. Reda, R.N. AbdelMessih, M. Steit, E.M. Mina, Thermal performance of domed roof in air-conditioned spaces, Energy Built. Environ. 5 (2024) 270–287, https://doi.org/10.1016/j.enbenv.2022.10.003.
[16] N.H. Wong, S.F. Tay, R. Wong, C.L. Ong, A. Sia, Life cycle cost analysis of rooftop gardens in Singapore, Build. Environ. 38 (2003) 499–509, https://doi.org/10.1016/S0360-1323(02)00131-2.
[17] E. Andreou, Thermal comfort in outdoor spaces and urban canyon microclimate, Renew. Energy 55 (2013) 182–188, https://doi.org/10.1016/j.renene.2012.12.040.
[18] E. Andreou, The effect of urban layout, street geometry and orientation on shading conditions in urban canyons in the mediterranean, Renew. Energy 63 (2014) 587–596, https://doi.org/10.1016/j.renene.2013.09.051.
[19] M. Taleghani, M. Tenpierik, A. van den Dobbelsteen, Indoor thermal comfort in urban courtyard block dwellings in the Netherlands, Build. Environ. 82 (2014) 566–579, https://doi.org/10.1016/j.buildenv.2014.09.028.
[20] O. Al-Hafith, S. B K, S. Bradbury, P. de Wilde, The impact of courtyard parameters on its shading level an experimental study in Baghdad, Iraq, Energy Proc. 134 (2017) 99–109, https://doi.org/10.1016/j.egypro.2017.09.539.
[21] X. He, W. Gao, R. Wang, Impact of urban morphology on the microclimate around elementary schools: a case study from Japan, Build. Environ. 206 (2021) 108383, https://doi.org/10.1016/j.buildenv.2021.108383.
[22] J. Zhu, J. Feng, J. Lu, Y. Chen, W. Li, P. Lian, X. Zhao, A review of the influence of courtyard geometry and orientation on microclimate, Build. Environ. 236 (2023) 110269, https://doi.org/10.1016/j.buildenv.2023.110269.
[23] L. Yang, X. Liu, F. Qian, S. Niu, Research on the wind environment and air quality of parallel courtyards in a university campus, Sustain. Cities Soc. 56 (2020) 102019, https://doi.org/10.1016/j.scs.2020.102019.
[24] R. Gunasekaran, R.S. Priya, Simulating the thermal efficiency of courtyard houses: new architectural insights from the warm and humid climate of tiruchirappalli city, India, Architecture 5 (2025) 21, https://doi.org/10.3390/architecture5020021.
[25] Q. Zhang, X. Ma, D. Xu, D. Zhou, Y. Yang, W. Jiang, The impact of courtyard spatial characteristics across historical periods on summer microclimates: a case study from China, Buildings 15 (2025) 224, https://doi.org/10.3390/buildings15020224.
[26] L. Marchi, J. Gaspari, K. Fabbri, Outdoor microclimate in courtyard buildings: impact of building perimeter configuration and tree density, Buildings 13 (2023) 2687, https://doi.org/10.3390/buildings13112687.
[27] H. Sun, J.S. Owen, S. Almazmumi, C. Liu, M. Mohammadi, A. Dik, C. Jimenez-Bescos, J.K. Calautit, Pollutant cross-transmission in courtyard buildings: wind tunnel experiments and computational fluid dynamics (CFD) evaluation, Build. Environ. 264 (2024) 111919, https://doi.org/10.1016/j.buildenv.2024.111919.
[28] H. Sun, H. Zhong, A. Dik, K. Ding, C. Jimenez-Bescos, J.K. Calautit, Numerical investigation of evaporative cooling strategies on the aero-thermal performance of courtyard buildings in hot-dry climates, Build. Environ. 258 (2024) 111588, https://doi.org/10.1016/j.buildenv.2024.111588.
[29] Q. Wen, H. Liu, Q. Zhou, Q. Guo, P. Wang, L. Zhang, The impact of ground-floor elevation of school buildings on courtyard wind environment, Buildings 14 (2024) 1146, https://doi.org/10.3390/buildings14041146.
[30] V.P. López-Cabeza, C. Rivera-Gómez, J. Roa-Fernández, M. Hernandez-Valencia, R. Herrera-Limones, Effect of thermal inertia and natural ventilation on user comfort in courtyards under warm summer conditions, Build. Environ. 228 (2023) 109812, https://doi.org/10.1016/j.buildenv.2022.109812.
[31] H.L. Gough, J.F. Barlow, Z. Luo, M.-F. King, C.H. Halios, C.S.B. Grimmond, Evaluating single-sided natural ventilation models against full-scale idealised measurements: impact of wind direction and turbulence, Build. Environ. 170 (2020) 106556, https://doi.org/10.1016/j.buildenv.2019.106556.
[32] H.-Y. Zhong, Y. Sun, J. Shang, F.-P. Qian, F.-Y. Zhao, H. Kikumoto, C. Jimenez-Bescos, X. Liu, Single-sided natural ventilation in buildings: a critical literature review, Build. Environ. 212 (2022) 108797, https://doi.org/10.1016/j.buildenv.2022.108797.
[33] A. Tablada, B. Blocken, J. Carmeliet, F. De Troyer, H. Verschure, The influence of courtyard geometry on air flow and thermal comfort: CFD and thermal comfort simulations, in: Proceedings of 22nd Conference on Passive and Low Energy Architecture, 2005, pp. 75–80.
[34] C. Tantasavasdi, N. Inprom, Impact of design features on natural ventilation of open-air malls in Thailand, Int. J. Low Carbon Technol. 16 (2021) 488–501, https://doi.org/10.1093/ijlct/ctaa080.
[35] O.S. Asfour, M.B. Gadi, Using CFD to investigate ventilation characteristics of vaults as wind-inducing devices in buildings, Appl. Energy 85 (2008) 1126–1140, https://doi.org/10.1016/j.apenergy.2007.10.015.
[36] J.I. Peren, T. Van Hooff, R. Ramponi, B. Blocken, B.C.C. Leite, Impact of roof geometry of an isolated leeward sawtooth roof building on cross-ventilation: straight, concave, hybrid or convex? J. Wind Eng. Ind. Aerod. 145 (2015) 102–114, https://doi.org/10.1016/j.jweia.2015.05.014.
[37] A. Zobaied, V.C. Tai, T.F. Go, P.L. Chong, L.K. Moey, Effect of gable roof with various roof pitches and obstacle heights on natural ventilation performance for an isolated building, JMES 16 (2022) 9033–9042, https://doi.org/10.15282/jmes.16.3.2022.06.0715.
[38] D. Prakash, Ventilation performance analysis on low-rise courtyard building for various courtyard shape factors and roof topology, Int. J. Vent. 22 (2023) 56–76, https://doi.org/10.1080/14733315.2022.2036477.
[39] M.F. Yassin, Impact of height and shape of building roof on air quality in urban street canyons, Atmos. Environ. 45 (2011) 5220–5229, https://doi.org/10.1016/j.atmosenv.2011.05.060.
[40] H.M. Khan, G.F. Lane-Serff, J. Dewsbury, Optimizing the design of courtyard houses for passive cooling in hot, dry regions, J. Build. Performance Simulat. 16 (2023) 231–247, https://doi.org/10.1080/19401493.2022.2134460.
[41] B. Wen, Q. Yang, F. Xu, J. Zhou, R. Zhang, Phenomenon of courtyards being roofed and its significance for building energy efficiency, Energy Build. 295 (2023) 113282, https://doi.org/10.1016/j.enbuild.2023.113282.
[42] Q. Yang, F. Xu, J.W. Lu, Z. Yang, Y. Bai, B. Wen, Green renovation and multi-objective optimization of Tibetan courtyard dwellings. https://doi.org/10.2139/ssrn.5004202, 2024.
[43] R. Bensalem, Wind-Driven Natural Ventilation in Courtyard and Atrium-type Buildings, University of Sheffield, 1991. PhD thesis, https://api.semanticscholar.org/CorpusID:106528234. (Accessed 13 July 2021).
[44] S. Sharples, R. Bensalem, Airflow in courtyard and atrium buildings in the urban environment: a wind tunnel study, Sol. Energy 70 (2001) 237–244, https://doi.org/10.1016/S0038-092X(00)00092-X.
[45] J.E. Cermak, J.A. Peterka, S.S. Ayad, M. Poreh, Passive and Hybrid Cooling Developments: Natural Ventilation: a wind-tunnel Study, 1981.
[46] P.-Y. Cui, Z. Li, W.-Q. Tao, Investigation of re -independence of turbulent flow and pollutant dispersion in urban street canyon using numerical wind tunnel (NWT) models, Int. J. Heat Mass Tran. 79 (2014) 176–188, https://doi.org/10.1016/j.ijheatmasstransfer.2014.07.096.
[47] [online], Ansys Fluent Theory Guide 2021R2, Ansys Inc., 2021, https://www.ansys.com/. (Accessed 20 January 2023).
[48] B.E. Launder, D.B. Spalding, The numerical computation of turbulent flows, Comput. Methods Appl. Mech. Eng. 3 (1974) 269–289, https://doi.org/10.1016/0045-7825(74)90029-2.
[49] V. Yakhot, S.A. Orszag, S. Thangam, T.B. Gatski, C. Speziale, Development of turbulence models for shear flows by a double expansion technique, Phys. Fluid. Fluid Dynam. 4 (1992) 1510–1520.

[50] T.-H. Shih, W.W. Liou, A. Shabbir, Z. Yang, J. Zhu, A new k-ϵ eddy viscosity model for high reynolds number turbulent flows, Comput. Fluid 24 (1995) 227–238, https://doi.org/10.1016/0045-7930(94)00032-T.
[51] D.C. Wilcox, Formulation of the k-w turbulence model revisited, AIAA J. 46 (2008) 2823–2838, https://doi.org/10.2514/1.36541.
[52] F.R. Menter, Review of the shear-stress transport turbulence model experience from an industrial perspective, Int. J. Comput. Fluid Dynam. 23 (2009) 305–316, https://doi.org/10.1080/10618560902773387.
[53] F.R. Menter, Two-equation eddy-viscosity turbulence models for engineering applications, AIAA J. 32 (1994) 1598–1605, https://doi.org/10.2514/3.12149.
[54] Nottingham, England, United Kingdom weather conditions, WeatherUnderground, (n.d.). https://www.wunderground.com/history/monthly/gb/derby/EGNX/date/2021-7 (accessed September 1, 2021).
[55] J.K. Calautit, D. O'Connor, P.W. Tien, S. Wei, C.A.J. Pantua, B. Hughes, Development of a natural ventilation windcatcher with passive heat recovery wheel for mild-cold climates: CFD and experimental analysis, Renew. Energy 160 (2020) 465–482.
[56] P.J. Roache, Perspective: a method for uniform reporting of grid refinement studies, J. Fluids Eng. Trans. Asme 116 (1994) 405–413.
[57] M.K. Esfeh, A. Sohankar, A.R. Shahsavari, M.R. Rastan, M. Ghodrat, M. Nili, Experimental and numerical evaluation of wind-driven natural ventilation of a curved roof for various wind angles, Build. Environ. 205 (2021) 108275, https://doi.org/10.1016/j.buildenv.2021.108275.